A Load Shedding Scheme for Inverter Based Microgrids

by

Alejandro P. Ojeda

S.B., E.E. M.I.T., 2010

Submitted to the Department of Electrical Engineering and Computer Science
in Partial Fulfillment of the Requirements for the Degree of
Master of Engineering in Electrical Engineering and Computer Science
at the Massachusetts Institute of Technology

May 2011
[June 2011]

Author_____
Department of Electrical Engineering and Computer Science
May 17, 2011

Certified by_____
James L. Kirtley, Jr.
Professor of Electrical Engineering
Thesis Supervisor

Accepted by_____
Dr. Christopher J. Terman
Chairman, Masters of Engineering Thesis Committee

A Load Shedding Scheme for Inverter Based Microgrids
by
Alejandro P. Ojeda

Submitted to the
Department of Electrical Engineering and Computer Science

May 17, 2011

In Partial Fulfillment of the Requirements for the Degree of
Master of Engineering in Electrical Engineering and Computer Science

ABSTRACT

Over the last decade, penetration of microgrids containing distributed generation (DG) sources has increased in grid distribution systems. This requires the stable operation of microgrids when connected to the distribution system as well as during islanding. Islanding that is fault provoked is more likely to cause unstable microgrid operation than planned islanding. During fault provoked islanding, unstable operation is exacerbated when induction motor (IM) loads are present. Using the *MATLAB* simulation tool *SimPowerSystems,* an inverter-based microgrid model connected to the IEEE-13 distribution system was created. A load shedding scheme was developed in order to improve microgrid stability during fault provoked islanding conditions.

Thesis Supervisor: James L. Kirtley, Jr.
Title: Professor of Electrical Engineering

Acknowledgments

I would like to thank Professor James Kirtley for his advice and supervision over the course of the project. I would also like to thank Dr. Hatem Zeineldin for his assistance and my family for their constant support and encouragement. Lastly, I would like to thank Nan McGarry for her support and invaluable help in editing and revising this document.

Contents

List of Figures

Chapter 1

Introduction

1.1 Microgrid

Over the past few decades, technological developments have enabled new forms of electricity production. The terms distributed generation, on-site generation, embedded generation, dispersed generation and decentralized generation all refer to a form of generating electricity from small energy resources. A common form of distributed generation is called cogeneration, which involves the simultaneous generation of electricity and useful heat. Many distributed generation (DG) resources use renewable energy such as wind or solar power to generate electricity. A cluster of DG units that can operate connected to the utility grid or in a stand-alone (islanded) mode is referred to as a microgrid.

The aim of a microgrid is to provide a value to both the utility and the customer by supplying power to local loads [1]. Some of the benefits associated with the integration of microgrids into the conventional utility grid are higher reliability of power distribution, reduction in environmental pollutants, higher power quality, and decreasing power line congestion. Common DG units in a microgrid are diesel generators, micro-turbines, fuel cells

and photovoltaic cells typically in the power range of 3kW to 10MW.

1.1.1 Typical Microgrid

A typical microgrid has DG units that incorporate the use of three phase synchronous or asynchronous machines to generate power. Since the voltage and current produced is alternating, transformers are needed to interface with the utility grid. The common types of microgrid power generation units commercially available at the time this document was written are as follows: Wind turbines, ranging from several kW to 5MW (typically found in groups at the same location), combustion turbines ranging from 500 kW to 25 MW and reciprocating engines ranging from 5kW to 7MW.

1.1.2 Inverter Based Microgrid

An inverter based microgrid has some DG units which produce DC current and voltage and therefore must incorporate a three phase power inverter and a coupling transformer in order to connect to the grid. A purely inverter based microgrid is one in which all of the DG units generate DC voltage and DC current that must be inverted to AC. Common inverter based power generation units commercially available at the time of this writing are as follows: Fuel cells ranging from 100 kW to 10MW (these include phosphoric acid fuel cells (PAFC), molten carbonate fuel cells (MCFC) and proton exchange membrane fuel cells (PEMFC)), photovoltaic systems in the size range of less than 1 kW to 100 kW and microturbines ranging from less than

25 kW to 500 kW. Figure 1-1 shows a cartoon of several inverter based microgrids connected to the utility grid.

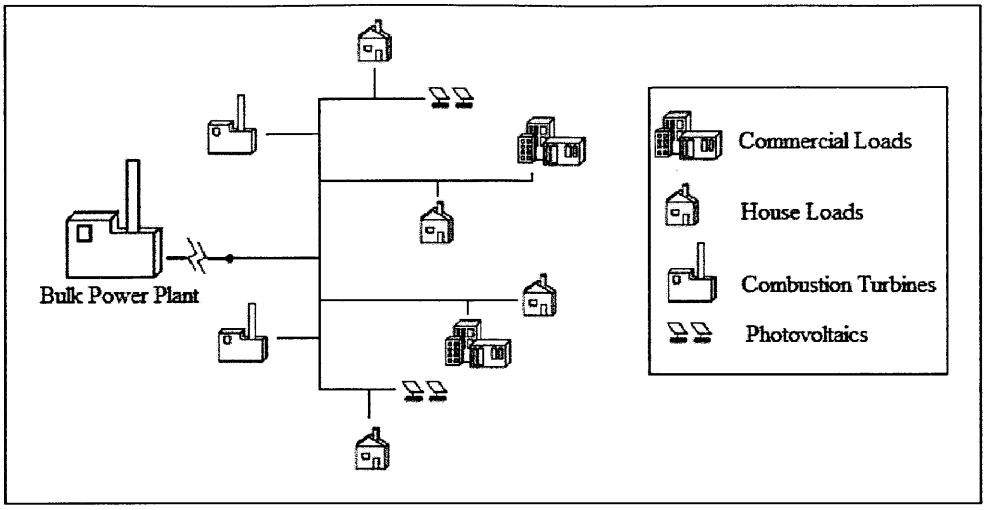

Figure 1-1: Grid Connected Inverter Based Microgrids

The presence of power electronics interfaces in inverter based DG units creates a situation in which the microgrid has very little or no moving parts. The inertia of the moving parts provides energy storage in the system. Therefore, a microgrid with larger inertia will have more transient stability in the moments subsequent to load connection or disturbances in the transmission lines. The dynamic behavior of a microgrid with little to no inertia is different from that of a typical microgrid that contains generators with rotating masses and larger inertia in the system. Microgrids with little inertia rely on energy storage in the form of battery storage to maintain stability during disturbances.

1.2 Islanding

Most of the microgrids in service today are connected to the main utility grid in order to provide power to the required loads. However, due to transient faults or disturbances that might occur in the utility transmission lines, the microgrid can become islanded by the action of the protection equipment. This type of islanding is termed unplanned or fault provoked islanding. Islanding which is planned by the utility is termed normal or planned islanding. By definition islanding occurs when part of a power system that contains DG units and loads becomes disconnected from the rest of the system and thus operates independently. In general, islanding is undesirable for two main reasons: it creates a safety hazard to personnel and creates the possibility of having the DG units out-of-phase with the main grid when reclosing occurs. Currently the IEEE Std. 929 and UL 1741 standards do not allow unplanned islanded operation of microgrids [2-3]. The IEEE standard 1547 requires the automatic detection and disconnection of all DG units during unplanned islanding conditions within a maximum time of 2 seconds [4]. A variety of passive, active, and hybrid methods for detecting microgrid islanding have been proposed in the literature [5]. Rapid islanding detection enables the circuit breakers which connect the DG units to the main utility grid to be tripped and allows for resynchronization at a later time when conditions permit. However, the IEEE P1547 standard also presents islanding as a topic for future research. Much of the recent literature concerning microgrids deals with microgrid operation and transient stability during islanding conditions based on different control schemes.

1.3 Prior Work

1.3.1 Control Schemes

A number of control modes for microgrids have been proposed in order to maintain the voltage and frequency stable and within the standard permissible levels. For inverter based microgrids, the control schemes aim at controlling the power electronic interfaces since it is not expected that fully controllable synchronous generators will be available during islanded conditions. Typically, either Voltage Source Inverter (VSI) control or PQ control is used to maintain line voltage and frequency stability [6]. The VSI control scheme is one in which the inverter acts as a voltage source with controlled magnitude and frequency. The PQ control scheme is one the inverter can be controlled to inject active and reactive power to maintain voltage magnitude and frequency.

Many microgrids contain more than one DG units. For such a situation, master/slave control schemes are typically used. One type of master/slave control scheme assumes one master DG unit and all the other DGs to be slaves. The master DG unit implements a VSI control scheme to set the reference microgrid voltage and frequency if islanding occurs. The slave inverters implement a PQ control scheme [7]. The implementation of these control schemes allows the microgrid to react to disturbances and situations that might cause islanding and maintain the stability of voltage and frequency. During an islanding situation, the control schemes maintain voltage and frequency stable by injecting or absorbing real and reactive power from energy storage resources.

1.3.2 Load Shedding

The control schemes described above do a fairly good job at maintaining microgrid voltage and frequency stable during disturbances, but they are reliant on the fact that the microgrid has enough storage capability to inject the power required for stabilization. When disconnection is not desired, load shedding is a common approach which has been used during situations when the microgrid lacks generation resources or storage energy to maintain the voltage and frequency stable during grid disconnection.

In essence, load shedding entails the disconnection of a specific amount of load (directly related to the source-to-load power unbalance) with the objective of preventing voltage and frequency degradation. A load shedding scheme acts whenever there is a disturbance in the system and acts to shed a certain amount of load based on specified thresholds. For microgrids with synchronous-based DG units, load shedding has been well studied and several load shedding schemes are proposed in the literature for both 60Hz and 50Hz systems [8]. The load shedding thresholds for these schemes are based on frequency, rate of change of frequency (ROCOF) or a combination of the two parameters. In [9] a system frequency response (SFR) model was developed from which a relation between the disturbance effect on the microgrid and the initial ROCOF value was developed.

$$Pstep = \frac{Hm}{30}\ [per\ unit] \tag{1.1}$$

Where H is the inertia of the microgrid, m is the initial value of the ROCOF after the disturbance, and Pstep is the effect of the disturbance on the microgrid. Using the Pstep a load shedding scheme was developed to more accurately shed load to maintain microgrid stability.

Even though there has been much research into load shedding, there is little in the literature regarding load shedding schemes for inverter based microgrids during fault provoked islanding. Moreover, the load shedding scheme in this study assumes that the microgrid contains variety of load types such as static loads and induction motor (IM) loads.

1.4 Objectives

The research objectives of this study are threefold. First, the dynamic behavior of the purely inverter based microgrid will be examined by using the *MatLab® Simulink®* simulation platform and compared to typical microgrid data in the literature. Second, the dynamic behavior of common microgrid loads will be modeled and examined in the *MatLab® Simulink®* simulation platform to determine their impact on the microgrid transient stability and on the line voltage and frequency. Third, using the aid of the simulation environment, a load shedding scheme for a specific purely inverter base microgrid will be developed in order to maintain line voltage and frequency stability when a grid disconnection occurs.

1.5 Overview

The material in this thesis will be presented in five chapters. Chapter 2 will describe the IEEE-13 node test feeder, which was used as a model for the utility grid to which the microgrid under study is connected to. Chapter 3 will contain an overview of typical microgrid loads and the models developed for simulation. In Chapter 4, the inverter based microgrid developed for simulation as well as its disturbance responses are discussed. Chapter 5 will present the inverter

based microgrid load shedding scheme to maintain line stability after grid disconnection. Chapter 6 includes a summary of the research as well as the conclusions reached.

Chapter 2

IEEE-13 Distribution Test Feeder

2.1 IEEE-13 Distribution Test Feeder

The first model we must develop for this study is a utility grid to which the inverter based microgrid can be initially connected. The IEEE Power Systems Society has published detailed data for several node test feeders. These test feeders were initially developed in order to provide developers of simulation software with a benchmark to test the accuracy and correctness of their power flow programs. However, this study will used the IEEE-13 distribution test feeder data [10] for modeling the static and dynamic behavior of the utility grid.

The IEEE-13 distribution test feeder was chosen to serve as the grid distribution system for this study because it has many important characteristics. The IEEE-13 feeder is 4.16kV and has fairly high loads. Its loads include both balanced and spot loads. The transmission lines in the IEEE-13 feeder include both overhead and underground lines. Most of the nodes contain shunt capacitors and one contains an in-line transformer. Even though the IEEE-13 feeder is not a very large distribution feeder, its important characteristics make it ideal for this study.

Figure 2-1 shows a one line diagram overview of the IEEE-13 distribution test feeder. The feeder contains two voltage regulating transformers, five different overhead transmission line configurations, two different underground line configurations, two different shunt capacitors, twelve transmission line segments, one circuit breaker, eight spot loads and one distributed load. All the configurations, parameters, and data used to model the IEEE-13 feeder for this study are listed in Appendix A.

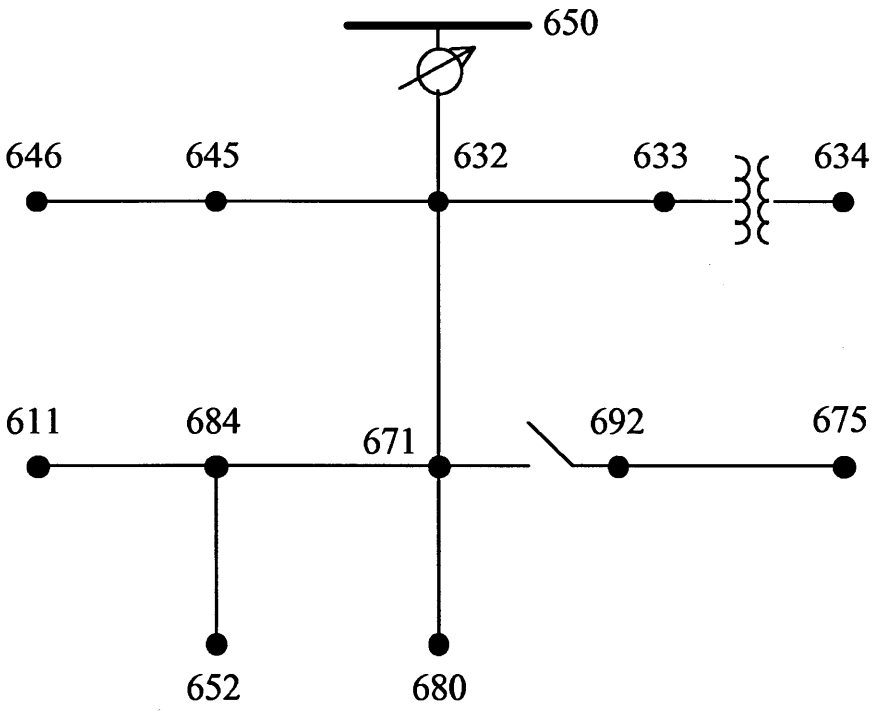

Figure 2-1: IEEE-13 Distribution Test Feeder [10]

2.2 MatLab Simulink Platform

The IEEE-13 feeder was modeled using the *MatLab*® *Simulink*® [11] simulation platform and the *SimPowerSystems* [12] tool bar. A major advantage of using the *MatLab*® *Simulink*® simulation platform is that it provides an interactive graphical environment with a

customizable set of libraries with which to design and simulate power systems. In the following subsections the component models of the IEEE-13 feeder will be described.

2.2.1 Transmission Lines

Transmission lines models were developed using the three phase PI section models in *SimPowerSystems*. Figure 2-2 shows one three phase PI section of the model, where Rs are the line resistances, Ls are the line inductances, Rm are the mutual resistances, Lm are the mutual inductances, Cp are the line capacitances and Cp are ground capacitance. These parameters are related to the positive and zero sequence impedance of the transmission line by equations 2.1-2.6 (where subscript1 denotes positive sequence and subscript 0 denotes zero sequence).

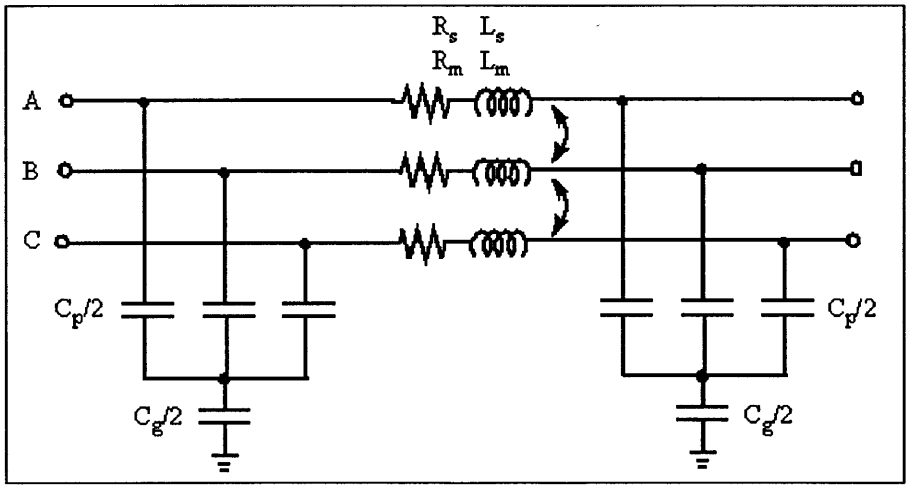

Figure 2-2: Three Phase PI Section Model in *SimPowerSystems* [12]

$$R_s = \frac{2 \cdot R_1 + R_0}{3} \tag{2.1}$$

$$R_m = \frac{R_0 - R_1}{3} \tag{2.2}$$

$$L_s = \frac{2 \cdot L_1 + L_0}{3} \tag{2.3}$$

$$L_m = \frac{L_0 - L_1}{3} \tag{2.4}$$

$$C_p = C_1 \tag{2.5}$$

$$C_g = \frac{3C_1 \cdot C_0}{(C_1 - C_0)} \tag{2.6}$$

In order to obtain the positive and zero sequence values, the impedance matrices for the transmission lines listed in Appendix A-1 were used. The matrices contained the transmission line configuration parameters. Equations 2.7-2.9 were used to obtain sequence parameters R_1, R_0, L_1, L_0, C_1 and C_0.

$$Zseq = A^{-1}ZA \tag{2.7}$$

$$A = \begin{matrix} 1 & 1 & 1 \\ 1 & a^2 & a \\ 1 & a & a^2 \end{matrix} \tag{2.8}$$

$$a = e^{j2\pi/3} \tag{2.9}$$

The single phase PI section model, which is a simplified model of the three-phase PI section discussed above, was used to model the single phase transmission lines.

2.2.2 Transformers

The IEEE-13 feeder contains two transformers. One is a voltage regulation three phase transformer that is placed immediately after the substation in a delta to wye configuration. The second transformer is a three phase step down transformer placed between nodes 633 and 634. To model these three phase transformers, a single phase transformer model was used in

SimPowerSystems. The transformer model is shown in figure 2-3. A single phase transformer was used for each line and connected as specified in Appendix A-2. The parameters for each three phase transformer are also listed in Appendix A-2.

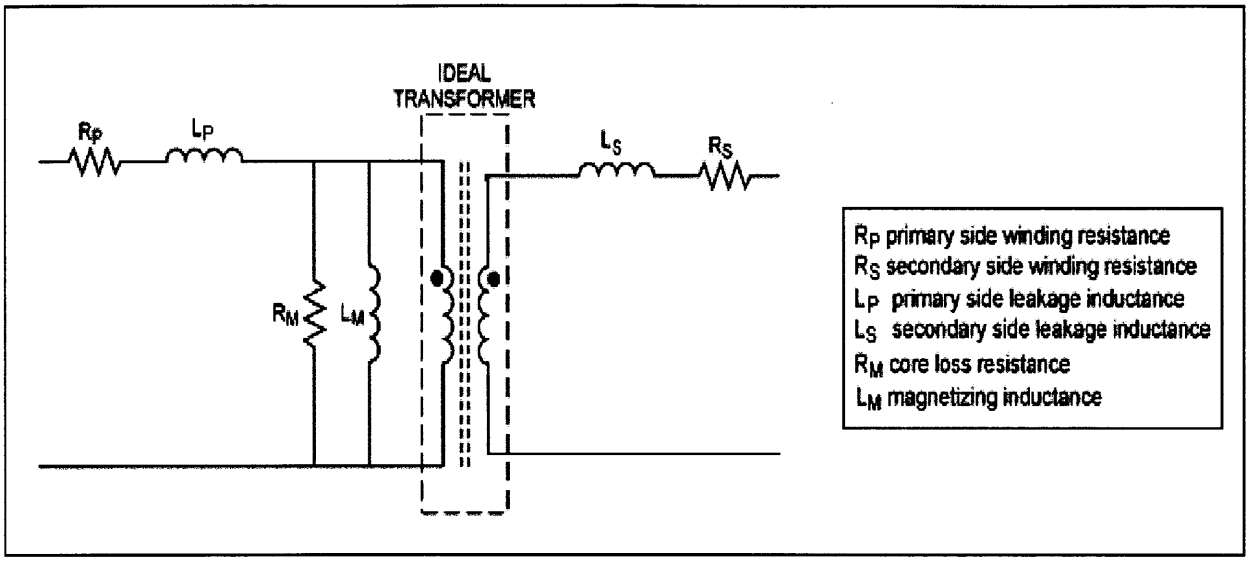

Figure 2-3: Single Phase Transformer Model

2.2.3 Shunt Capacitors

In order to model the shunt capacitors in the nodes, the three-phase the parallel RLC model in *SimPowerSystems* was used. The resistance value was set to zero, the capacitance to infinity and the frequency to 60 Hz. The capacitor voltage and reactive power were dependent on the node location and are listed in Appendix A-3. To calculate the capacitance value the following relation was used:

$$C = \frac{Q}{(wV^2)} \tag{2.10}$$

Where V is the capacitor voltage in [volts], w the line frequency in [rad/s] and Q the reactive power in [VAr].

2.2.4 Distribution Loads

The IEEE-13 feeder consists of three types of spot loads in both wye and delta connections: constants real and reactive power (PQ), constant impedance and constant current. The feeder also contains one distributed load along the 632-671 distribution line.

In order to model constant impedance loads, single-phase RLC load models in *SimPowerSystems* were used. This was done because not all the spot loads in the IEEE-13 feeder are three-phase, and the spot loads that are three-phase all contain different real and reactive power values in each phase. The nominal frequency is 60 Hz and the nominal voltage is dependent on the connection type (wye or delta) and on the specific node the spot load is connected to. The real and reactive power of the loads were set given the data in Appendix A-4.

In order to model a constant real and reactive power (PQ) load in *SimPowerSystems*, single-phase RLC load models were again used because no single phase model for constant real and reactive power (PQ) loads exists in *SimPowerSystems*. We can however ensure that the real and reactive power values drawn from each PQ spot load are those specified in Appendix A-4 by appropriately adjusting voltage of the RLC load model. The RLC model voltage is dependent on the voltage on the specific node that the spot load is connected to (for example, 480V line to line at node 634). The radial power flow analysis of the IEEE-13 in [10] specifies what the voltage must be at a specific node in per unit values. Therefore, we can scale the RLC model voltage by

the per unit value at each specific node in order to guarantee that the power drawn by the PQ load at steady state is equal to the specified values in the Appendix. For the example above, the voltage of each RLC load model would be scaled by .9940, 1.0218 and .9960 at phases A, B and C, respectively.

For the case of constant current load, the same problem arises as in the PQ load case. A similar approach is taken in order to model a constant current load using single-phase RLC load models in *SimPowerSystems*. At each node the spot loads are connected to, the voltage as well as the real and reactive power for each RLC load model are all scaled by their corresponding per unit value. This ensures that the correct current value is drawn from the each load at steady state conditions.

The distributed load between node 632 and 671 was lumped into two spot loads. Two-thirds of the total distributed load was place one-fourth down the length of the line. The other one-third of the load was placed at the end of the line at node 671. Figure 2-3 shows a cartoon of the distributed load lumped into spot loads along the transmission line.

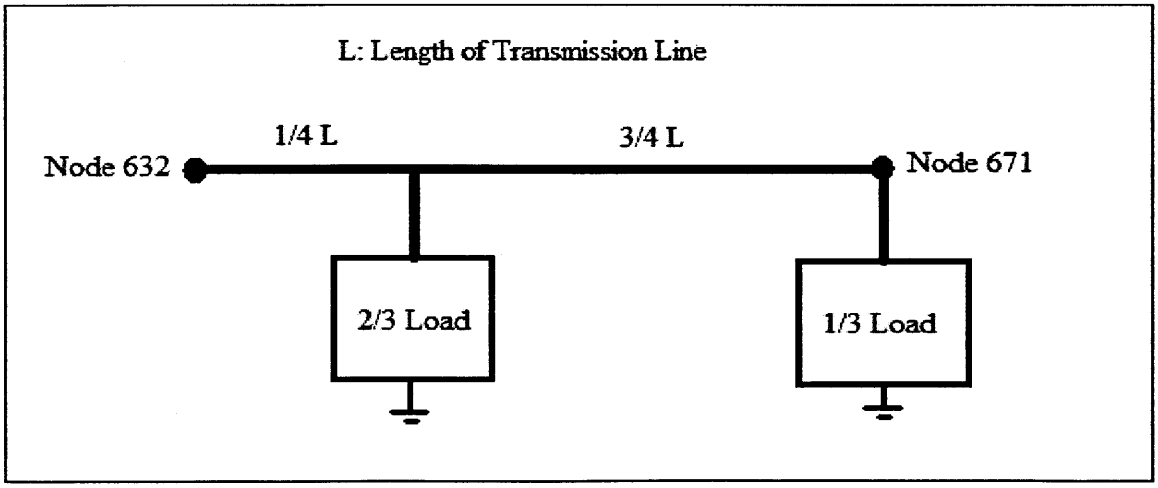

Figure 2-4: Lumped Distributed Load

2.2.5 Protective Device

The IEEE-13 feeder contains one protective device between nodes 671 and 692. This device is a three-phase circuit breaker. The three-phase circuit breaker model in *SimPowerSystems* was used to model this. An on state resistance of .001 Ohms per phase as well as a 1 MOhm parallel snubber resistance per phase was included in the model.

2.3 Steady-State Comparison

In order to determine the accuracy of the IEEE-13 model that was developed, both steady-state voltage and angle were calculated at each node for each phase in the feeder. These values are displayed in figure 2-5. The values obtained were then compared to the voltage profile values in Appendix A-5 and their percent errors were calculated and are displayed in figure 2-6. The highest percent error was 2.5% in the voltage in phase A of node 652. In general phase A had the high percentage errors in steady-state voltage, although most error values were under 1% overall. Nevertheless, these errors are within acceptable margins for this study.

Node	Mag (pu)	Angle (deg.)	Mag (pu)	Angle (deg.)	Mag (pu)	Angle (deg.)
	A-N	A-N	B-N	B-N	C-N	C-N
650	1	0	1	-120	1	120
RG60	1.0435	-2.00E-03	1.05	-120.003	1.0527	119.965
632	1.0249	-2.48	1.0448	-121	1.0089	118.82
633	1.0238	-2.54	1.0442	-121.02	1.0081	118.82
XFXFM1	1.0078	-3.2	1.0312	-121.34	0.9956	118.5
634	1.0078	-3.2	1.0312	-121.34	0.9956	118.5
645			1.0396	-121.17	1.0058	118.87
646			1.0379	-121.25	1.0037	118.91
671	1.01	-5.31	1.0482	-121.3	0.9942	117.9
680	1.01	-5.31	1.0482	-121.25	0.9942	117.9
684	1.0093	-5.27			0.9935	117.87
611					0.9929	117.82
652	1.0074	-5.21				
692	1.01	-5.3	1.0483	-121.3	0.9941	117.9

Figure 2-5: Steady-State Voltages and Angles of IEEE-13 Model

Node	Mag	Angle	Mag	Angle	Mag	Angle
	% error	% error	% error	% error	% error	% error
	A-N	A-N	B-N	B-N	C-N	C-N
650	0	0	0	0	0	0
RG60	1.788235	0.2	0	0.0025	1.497146	0.029167
632	0.381978	0.401606	0.268714	0.5884	0.835463	0.840193
633	0.569745	0.78125	0.394193	0.615915	0.660229	0.848752
XFXFM1	1.378131	0.928793	0.919945	0.720013	0.040161	0.979974
634	1.38833	0.928793	0.919945	0.720013	0.040161	0.98858
645	N/A	N/A	0.648659	0.598852	0.955194	0.856949
646	N/A	N/A	0.65949	0.598459	0.957174	0.856658
671	2.020202	0.188679	0.446386	0.85009	1.677235	1.62041
680	2.020202	0.188679	0.446386	0.89096	1.677235	1.62041
684	2.145532	0.93985	N/A	N/A	1.813896	1.682195
611	N/A	N/A	N/A	N/A	1.961388	1.761962
652	2.534351	0.761905	N/A	N/A	N/A	N/A
692	2.020202	0.188324	0.436889	0.85009	1.677406	1.62041

Figure 2-6: Model Percent Errors

This chapter described how the model of the IEEE-13 node test feeder for the *MatLab*® *Simulink*® simulation environment was developed. This involved the use of data from [10] to develop models for the transmission lines, loads, shunt capacitors and protective devices of the IEEE-13 feeder. The IEEE-13 bus distribution feeder acts as a grid to which the microgrid can be connected to.

Chapter 3

Microgrid Loads

Power system engineers make decisions on the development or reinforcement of power systems based largely on simulation analyses. Consequently, costly operational limitations might be incurred by the utility if these analyses are inaccurate. Over the years, more attention has been given to modeling generation and transmission systems than to system loads. Historically, load modeling has been quite challenging for various reasons. Some of these include the lack of precise knowledge of load compositions, the large number and diversity of load components and the changing of load composition through time. However, studies have shown that simulation results can be significantly impacted when better load models are used [13]. Therefore, it is just as important to accurately model loads as it is to model generation sources and transmission networks. In general, the load characteristics of a given system should be identified in order use models appropriately in simulation studies.

In this section of the study, we aim to create accurate models for three major load types: static and induction motor loads. These loads are very common in load classes such as residential, commercial and industrial, which a typical microgrid might be built to supply power to.

3.1 Static Loads

Static loads are those loads in which their active and reactive powers are functions of bus voltage and frequency at any given time. The exponential model [14] is a load model that relates power to voltage as shown in equations 3.1 and 3.2.

$$P = P_0\left(\frac{V}{V_0}\right)^{np} \tag{3.1}$$

$$Q = Q_0\left(\frac{V}{V_0}\right)^{nq} \tag{3.2}$$

Where P is the real power, Q is the reactive power, P_o is the real power consumed at rated voltage, Q_o is the reactive power consumed at rated voltage, V is the bus voltage, V_o is the rated voltage and np and nq are load model parameters. The advantage of using this model is that constant power, constant current, and constant impedance models can be developed by simply changing the exponent power in the model. That is, for a constant power load np=nq=0, for a constant current load np=nq=1 and for a constant impedance load np=nq=2.

From residential to industrial load classes, loads exhibiting the above characteristics are ubiquitous. For example, incandescent lighting can be modeled as a constant impedance type load (np=nq=2). However, due to temperature changes in the filament, the resistance changes and the voltage variation exhibited is np=nq=1.55 [14]. Thermostat controlled loads - such as space heaters, water heaters, soldering machines, etc. – may consume 20 to 40 percent of the system load in residential, commercial and industrial load classes. Thermostat loads exhibit constant impedance characteristics in the short term, but constant power characteristics for long term simulations [14]. Discharge lighting used for parking and street lighting can consume

around 20 percent of commercial loads. These fluorescent, mercury, or sodium type discharge loads behave mostly as constant current loads (np=nq=1). Manually controlled loads – such as cooking stove loads – can behave as constant impedance or constant power loads.

If a static load is frequency dependent, then a line frequency dependence term can be added to these static models. To do this we can make use of the frequency dependent load model in [14]. Equations 3.3 and 3.4 show the static load models with both voltage and frequency dependence terms.

$$P = P_0\left(\frac{V}{V_0}\right)^{np} \cdot (1 + a_p(f - f_0)) \tag{3.3}$$

$$Q = Q_0\left(\frac{V}{V_0}\right)^{nq} \cdot \left(1 + a_q(f - f_0)\right) \tag{3.4}$$

Where f is the line frequency, f_0 is the rated frequency, and a_p and aq are frequency sensitivity parameters in the model..

3.2 Induction Motor Loads

Nearly all large electrical machinery, fans, pumps, etc., use induction motors. Induction motor (IM) loads consume around 70 percent of the electrical energy in the Unites States and it is very likely that a typical microgrid would power IM type loads. This is especially true if the microgrid load class is industrial. As emphasized in [13], the need for dynamic modeling of IM loads is vital to simulated voltage stability studies.

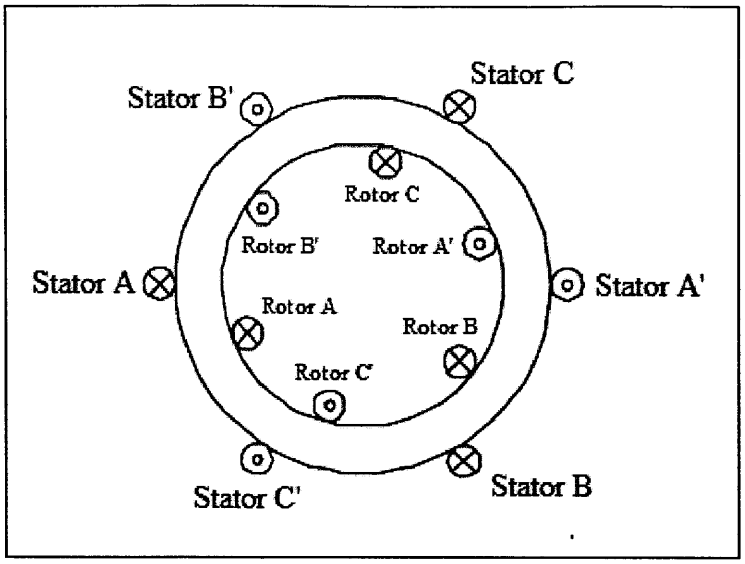

Figure 3-1: Cross Section of a Symmetrical Three-Phase Motor

The stator voltages of a three-phase induction machine in a stationary reference frame can be modeled as follows:

$$V_{sa}(t) = R_s i_{sa}(t) + \frac{d\Phi_{sa}(t)}{dt} \tag{3.5}$$

$$V_{sb}(t) = R_s i_{sb}(t) + \frac{d\Phi_{sb}(t)}{dt} \tag{3.6}$$

$$V_{sc}(t) = R_s i_{sc}(t) + \frac{d\Phi_{sc}(t)}{dt} \tag{3.7}$$

Where the resistance (R_s) in each phase are assumed to be equal, i_{sx} denotes the stator current in a given phase x, and Φ_{sx} denotes the stator flux linkage in a given phase x.

The stator voltages of a three-phase induction machine in a stationary reference frame can similarly be modeled as follows:

$$V_{ra}(t) = R_r i_{ra}(t) + \frac{d\Phi_{ra}(t)}{dt} \tag{3.8}$$

$$V_{rb}(t) = R_r i_{rb}(t) + \frac{d\Phi_{rb}(t)}{dt} \tag{3.9}$$

$$V_{rc}(t) = R_r i_{rc}(t) + \frac{d\Phi_{rc}(t)}{dt} \tag{3.10}$$

Where the resistance (Rr) in each phase are assumed to be equal, i_{rx} denotes the rotor current in a given phase x, and Φ_{rx} denotes the rotor flux linkage in a given phase x.

For algebraic simplicity in building the model, we can change the reference frame to a rotating coordinate system. This is done by applying Park's Transformation (listed as equation 3.11) to the stationary reference frame voltages in equation 3.5 to 3.10. This transformation then gives the stator and rotor voltages in the familiar d,q reference frame. Circuit models of the induction machine stator and rotor are shown in figures 3-3 and 3-4.

$$P = \left(\frac{2}{3}\right)\begin{bmatrix} \cos(\theta) & \cos\left(\theta - \frac{2\pi}{3}\right) & \cos\left(\theta + \frac{2\pi}{3}\right) \\ \sin(\theta) & \sin\left(\theta - \frac{2\pi}{3}\right) & \sin\left(\theta + \frac{2\pi}{3}\right) \\ \frac{1}{2} & \frac{1}{2} & \frac{1}{2} \end{bmatrix} \tag{3.11}$$

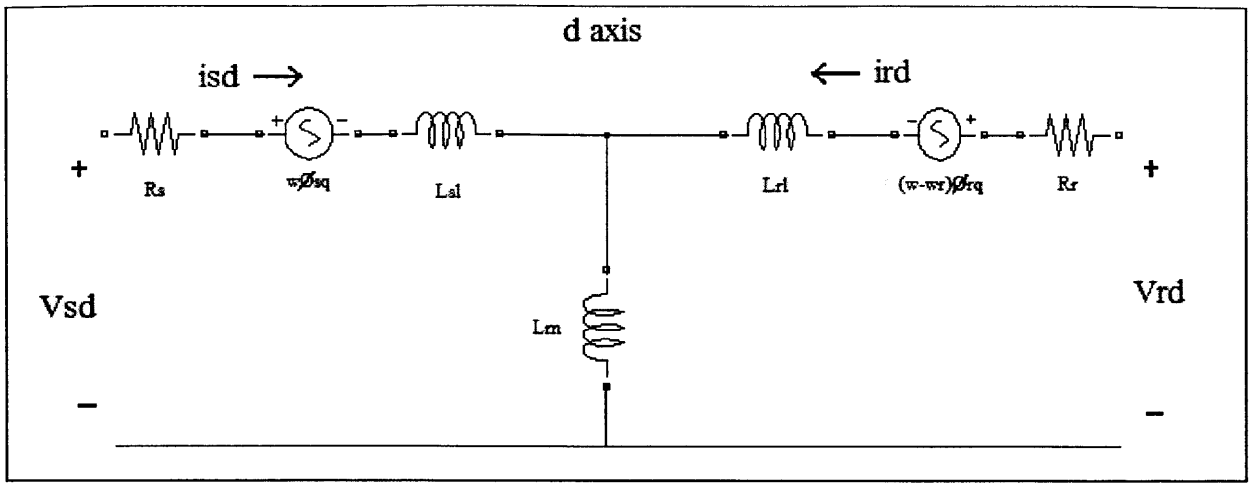

Figure 3-2: D-axis Stator and Rotor Circuit Diagram

The stator and rotor voltage equations in the d-axis reference are as follows:

$$V_{sd} = R_s i_{sd} + \frac{d\Phi_{sd}}{dt} - w\Phi_{sq} \tag{3.12}$$

$$V_{rd} = R_r i_{rd} + \frac{d\Phi_{rd}}{dt} - (w - w_r)\Phi_{rq} \tag{3.13}$$

Where Rs is the stator resistance, i_{sd} is the d-axis stator current, Φ_{sd} is the d-axis stator flux, w is a given angular velocity, Φ_{sq} is the q-axis stator flux, R_r is the rotor resistance, i_{rd} is the d-axis rotor current, Φ_{rd} is the d-axis rotor flux, Φ_{rq} is the q-axis rotor flux and w_m is the angular velocity of the rotor.

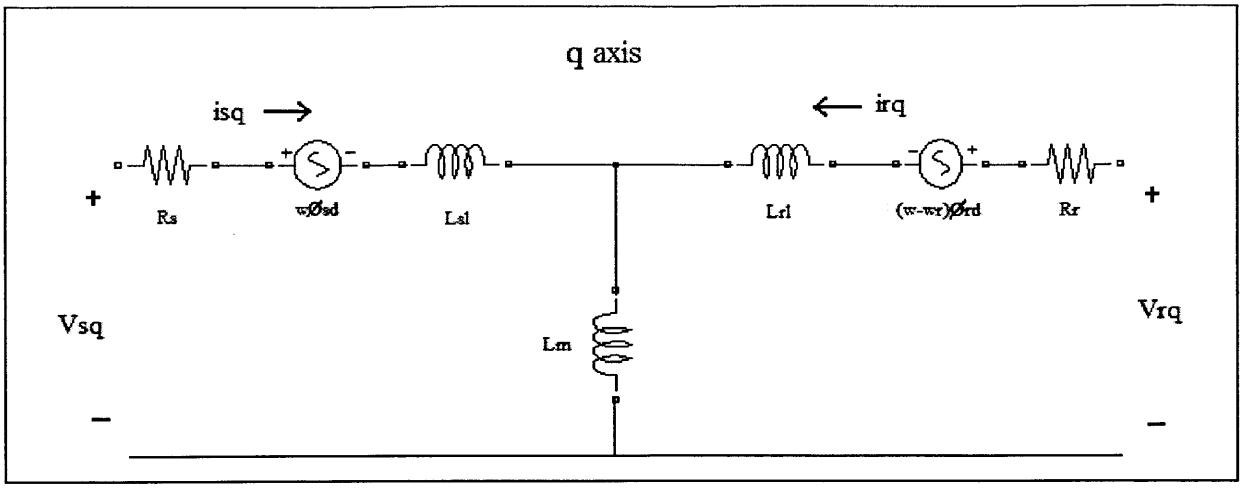

Figure 3-3: Q-axis Stator and Rotor Circuit Diagram

The stator and rotor voltage equations in the q-axis reference are as follows:

$$V_{sq} = R_s i_{sq} + \frac{d\Phi_{sq}}{dt} + w\Phi_{sd} \tag{3.14}$$

$$V_{rq} = R_r i_{rq} + \frac{d\Phi_{rq}}{dt} + (w - w_r)\Phi_{rd} \tag{3.15}$$

Where i_{sq} is the q-axis stator current and i_{rq} is the q-axis rotor current.

Moreover, the stator and rotor fluxes in both the d-axis and the q-axis are related to current and inductance as shown in equations 3.16 to 3.21.

$$\Phi_{sd} = L_s i_{sd} + L_m i_{rd} \tag{3.16}$$

$$\Phi_{rd} = L_r i_{rd} + L_m i_{sd} \tag{3.17}$$

$$\Phi_{sq} = L_s i_{sq} + L_m i_{rq} \tag{3.18}$$

$$\Phi_{rq} = L_r i_{rq} + L_m i_{sq} \tag{3.19}$$

$$L_s = L_{sl} + L_m \tag{3.20}$$

$$L_r = L_{rl} + L_m \tag{3.21}$$

Where Lm is the magnetizing inductance, L_{sl} is the stator leakage inductance and L_{rl} is the rotor leakage inductance.

These equations can be written in matrix notation as follows:

$$\begin{bmatrix} V_{sd} \\ V_{sq} \\ V_{rd} \\ V_{rq} \end{bmatrix} = \begin{bmatrix} R_s + \frac{dL_s}{dt} & -wL_s & \frac{dL_m}{dt} & -wL_m \\ wL_s & R_s + \frac{dL_s}{dt} & wL_m & \frac{dL_m}{dt} \\ \frac{dL_m}{dt} & -(w - w_r)L_m & R_r + \frac{dL_r}{dt} & -(w - w_r)L_r \\ (w - w_r)L_m & \frac{dL_m}{dt} & (w - w_r)L_r & R_r + \frac{dL_r}{dt} \end{bmatrix} \cdot \begin{bmatrix} i_{sd} \\ i_{sq} \\ i_{rd} \\ i_{rq} \end{bmatrix} \tag{3.22}$$

If the angular frequency of the machine w is equal to w_r (referenced to the rotor) equation 3.22 simplifies to equation 3.23.

$$\begin{bmatrix} V_{sd} \\ V_{sq} \\ V_{rd} \\ V_{rq} \end{bmatrix} = \begin{bmatrix} R_s + \frac{dL_s}{dt} & -wL_s & \frac{dL_m}{dt} & -wL_m \\ wL_s & R_s + \frac{dL_s}{dt} & wL_m & \frac{dL_m}{dt} \\ \frac{dL_m}{dt} & 0 & R_r + \frac{dL_r}{dt} & 0 \\ 0 & \frac{dL_m}{dt} & 0 & R_r + \frac{dL_r}{dt} \end{bmatrix} \cdot \begin{bmatrix} i_{sd} \\ i_{sq} \\ i_{rd} \\ i_{rq} \end{bmatrix} \tag{3.23}$$

To a second accuracy, the dynamics of the mechanical parts of an induction motor can be modeled as follows:

$$\frac{d\theta_m}{dt} = w_m \tag{3.24}$$

$$\frac{dw_m}{dt} = \frac{T_e - Fw_m - T_m}{2H} \tag{3.25}$$

Where Θ_m is the angular position of the rotor, w_m is the angular velocity of the rotor, Te is the electromagnetic torque, F is the combined rotor and load viscous coefficient, Tm is the shaft torque and H is the combined rotor and load inertia constant. The electromagnetic torque has a relation to the electrical parameters shown in equation 3.26.

$$T_e = \left(\frac{3}{2}\right) p(\Phi_{sd} i_{sq} - \Phi_{sq} i_{sd}) \tag{3.26}$$

Where p is the number of pole pairs of the machine.

The induction motor model described above assumes symmetrical three phase windings and neglects iron losses. The model also assumes that the stator and rotor windings are multi turn full pitch coils on the sides of the air gap [15]. Nevertheless, the model captures dynamic effects in steady-state and transient conditions that are important in analyzing the effects IM loads have on microgrid line frequency and voltage.

Chapter 4

Inverter-Based Microgrid Model

In this chapter, the inverter-based microgrid model is presented. It is followed by a presentation of a selected number of simulation plots that depict important findings. The chapter concludes with a discussion of these results.

4.1 Microgrid Model Overview

The inverter-based microgrid model is made up of four main parts: a power source, an inverter with its control system, a line filter and a coupling transformer. Figure 4-1 shows a cartoon of the microgrid. The microgrid is connected to node 680 of the IEEE-13 feeder. There is a three phase breaker between node 680 and the microgrid which allowed grid transients and disconnects to be simulated.

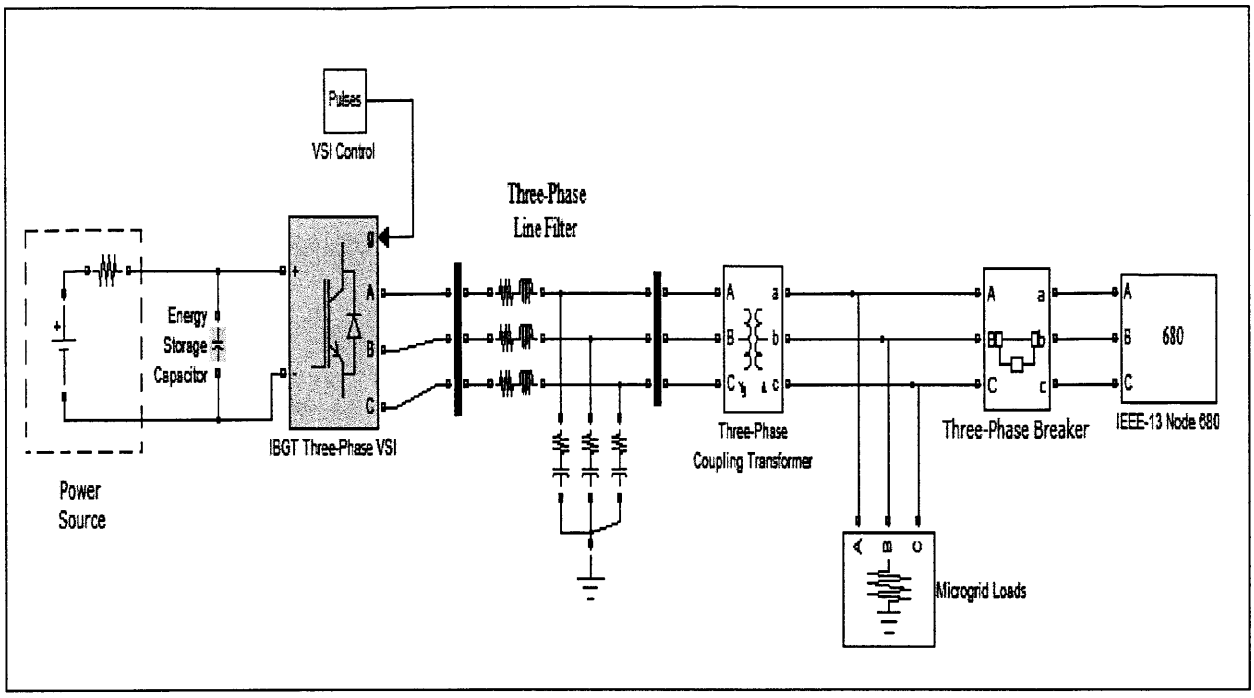

Figure 4-1: Inverter-Based Microgrid Overview

4.1.1 Power Source

The power source used for this study was a simple DC voltage source with an internal resistance. The DC voltage source is rated at 679 V DC and the current is limited such that the power drawn from the source is limited to 50 kW. This is one of the simplest types of models that can be used while still preserving interesting dynamic behavior. If desired, the power source can also be replaced with PV array or fuel cell models.

In order to balance the difference between the instantaneous and average power, an energy storage or DC link capacitor was placed between the power source and the inverter.

4.1.2 Inverter and Control

An electrical diagram of the inverter model is shown in figure 4-2. The inverter is a three-phase, full-wave bridge, voltage source inverter (VSI). Since it is a VSI, power reversal takes place through the reversal of the current polarity. It contains three totem poles with two IGBTs and two diodes each. The IGBTs are numbered 1-6 and the diodes are numbered 1'-6'. The on resistance of the switch is 0.001 Ohm. Each IGBT has a forward voltage of 1 V and each diode has a forward voltage of 0.8 V. The capacitor shown in figure 4-2 is the energy storage capacitor described above.

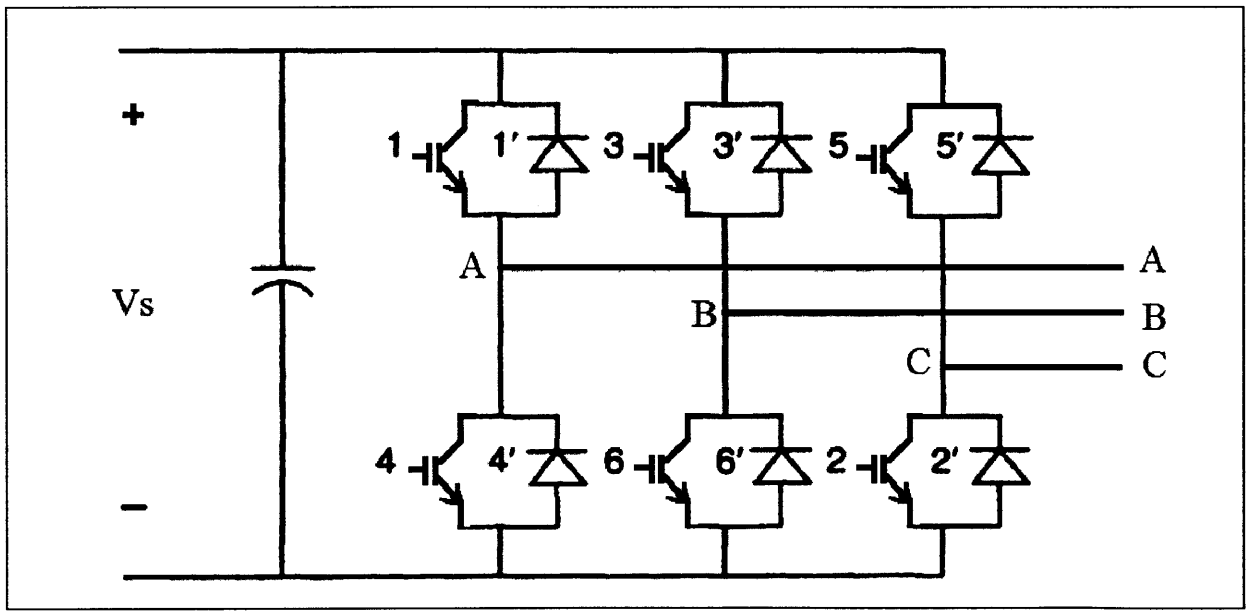

Figure 4-2: Three-Phase, Full Bridge VSI

A cartoon of the control system for the inverter is shown in figure 4-3. The control scheme consists of two loops, namely an inner current control loop and an outer power control loop.

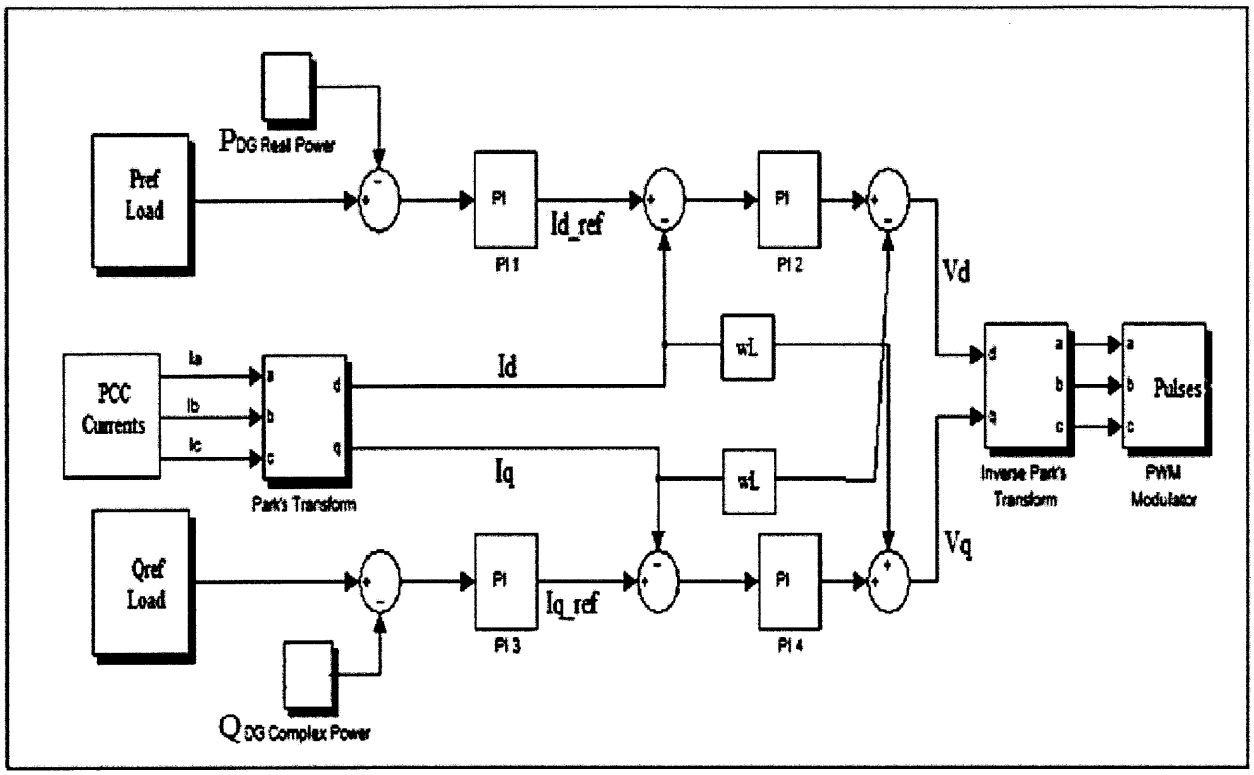

Figure 4-3: Inverter Control Scheme

The outer loop sets the real and complex power reference points (P_{ref} and Q_{ref}) for the DG unit. The DG must have these values set properly in order to properly supply power to the grid and/or loads and maintain the line voltage and frequency stable. In general, voltage support is linked to the reactive power delivered and frequency support is linked to the real power delivered. The P_{ref} and Q_{ref} are compared with the current real and reactive power out of the DG (P_{DG} and Q_{DG}). The difference in the reference and real time values are passed through proportional plus integral (PI) controllers. The

outputs of the PI_1 and PI_3 controllers become the direct-axis and quadrature-axis current reference for the inner loop, respectively. Appendix sections B-1 and B-2 show how to obtain the real and complex DG values and give the proportional and integral gains used for each PI controller.

The inner loop uses fast current control to inject the appropriate amount of current and achieve desired reference values. In order to see the why the structure of the inner loop is as it is illustrated in figure 4-3, we can do a simple Kirchhoff's voltage loop from the output of the inverter to the input of the coupling transformer. We obtain:

$$V_{ga} = V_a - \left(L\frac{d}{dt}I_a + RI_a\right) \tag{4.1}$$

$$V_{gb} = V_b - \left(L\frac{d}{dt}I_b + RI_b\right) \tag{4.2}$$

$$V_{gc} = V_c - \left(L\frac{d}{dt}I_c + RI_c\right) \tag{4.3}$$

Where Vgx represents the voltage at the coupling transformer in phase x, Vx is the voltage at the output of the inverter in phase x, Ix is the current in phase x, L and R are the inductance and resistance per phase, respectively. Using Park's Transportation we can transform equations 4.1-4.3 into a rotating reference frame.

$$V_{gd} = V_d - \left(L\frac{d}{dt}I_d + RI_d\right) + wLI_q \tag{4.4}$$

$$V_{gq} = V_q - \left(L\frac{d}{dt}I_q + RI_q\right) - wLI_d \tag{4.5}$$

Where w is the grid frequency. Using feedback and PI compensators to provide decoupled current control yields equations 4.6-4.7.

$$V_d = (K_p + \frac{K_I}{s})(I_{d,ref} - I_d) - wL'I_q \quad (4.6)$$

$$V_q = (K_p + \frac{K_I}{s})(I_{q,ref} - I_q) + wL'I_d \quad (4.7)$$

Where K_p represents the proportional gain and K_I represents the integral gain of the PI controller. In short, the inner loop takes the $I_{d,ref}$ and $I_{q,ref}$ values from the outer loop and compares them to the point of common coupling (PCC) I_d and I_q values, respectively. The PCC I_d and I_q values are obtained by applying Park's Transform (listed as equation 3.11) to line currents I_a, I_b and I_c measured at the PCC. The V_d and V_q values are obtained by summing each respective PI output and cross term. The inverse Park's Transform is then applied to the V_d and V_q values to obtain line voltages V_a, V_b and V_c. These line voltages are then fed to a PWM modulator that generates the inverter switching signals.

4.1.3 Filter

Between the inverter output and the coupling transformer is a three-phase LC filter. The filter is shown in Figure 4-1. The inductance and capacitance values per phase are 800 uH and 30 uF, respectively. The cutoff frequency for this filter is approximately 1027 Hz. Moreover, there is a small resistor (of value 4mOhm) in series with the inductor in each phase which represents line resistance. The main purpose of the LC filter is to reduce current harmonics delivered to the microgrid loads and/or the grid, especially higher order harmonics near the switching frequency

of the control system. This in turn helps to reduce the total harmonic distortion delivered to loads and/or the grid.

4.1.4 Coupling Transformer

The coupling transformer between the inverter output and node 680 of the IEEE-13 feeder is a three-phase step-up transformer. The transformer model for a single phase is shown in figure 2-3. The parameters for this transformer are as follows:

Nominal Power: 1 MVA

Nominal Frequency: 60 Hz

Primary Voltage RMS, line-line: 480 Vrms

Primary Inductance: 0.0008 p.u.

Primary Resistance: 0.02 p.u.

Secondary Voltage RMS, line-line: 4160 Vrms

Secondary Inductance: 0.0008 p.u.

Secondary Resistance: 0.02 p.u.

Magnetizing Inductance: 100 p.u.

Magnetizing Resistance: 100 p.u.

The coupling transformer serves two purposes. The first is to increase the output voltage of the microgrid to 4.16 kV, RMS line-line to match the line-line voltage at node 680. Second, like the LC filter, the inductance from the transformer windings ensures that the DC energy storage capacitor does not discharge into the transmission lines and also reduces the harmonic current flow.

4.2 Planned Islanding Simulations

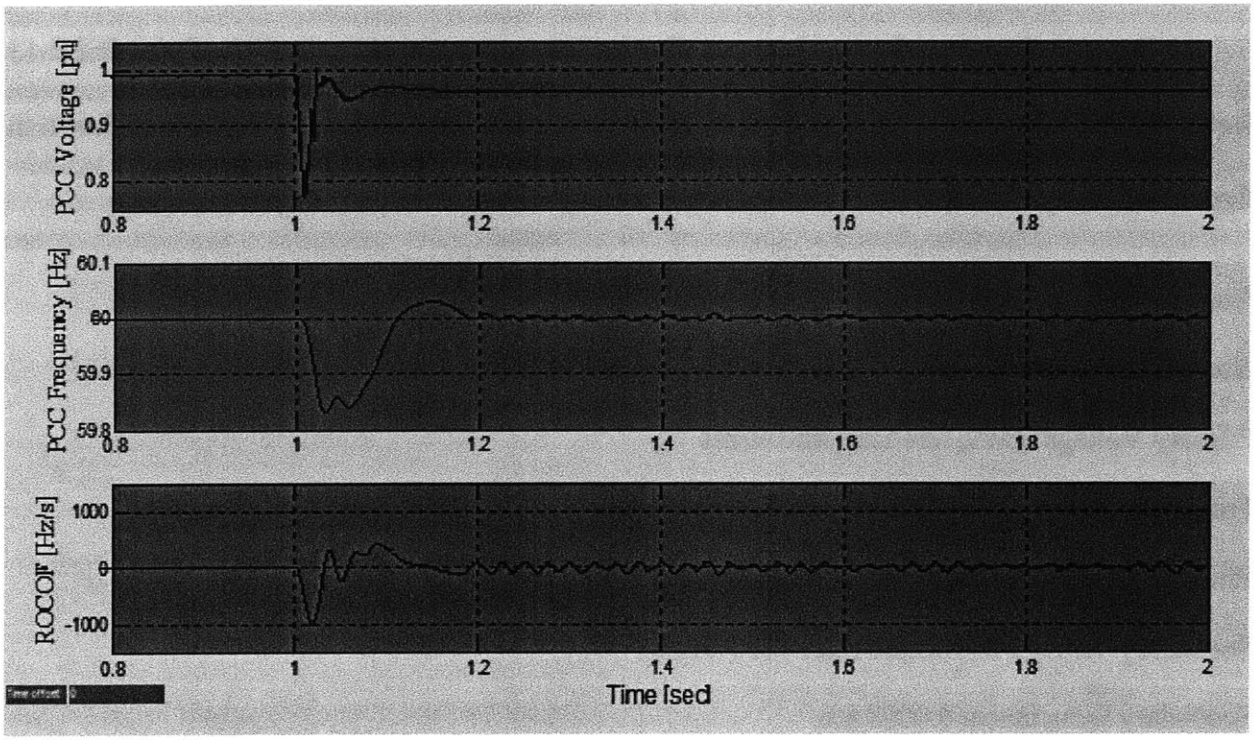

Figure 4-4: Voltage, Frequency and ROCOF subject to 50 kVa Constant Power Load

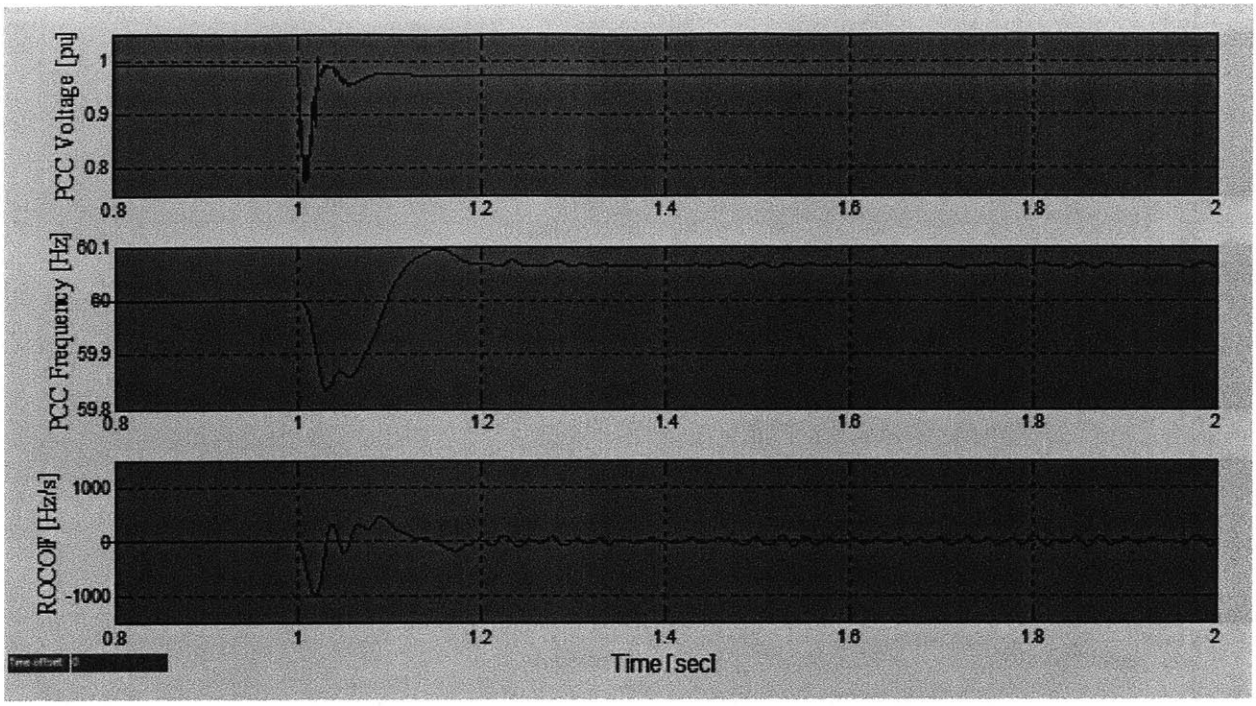

Figure 4-5: Voltage, Frequency and ROCOF subject to 50 kVa Constant Current Load

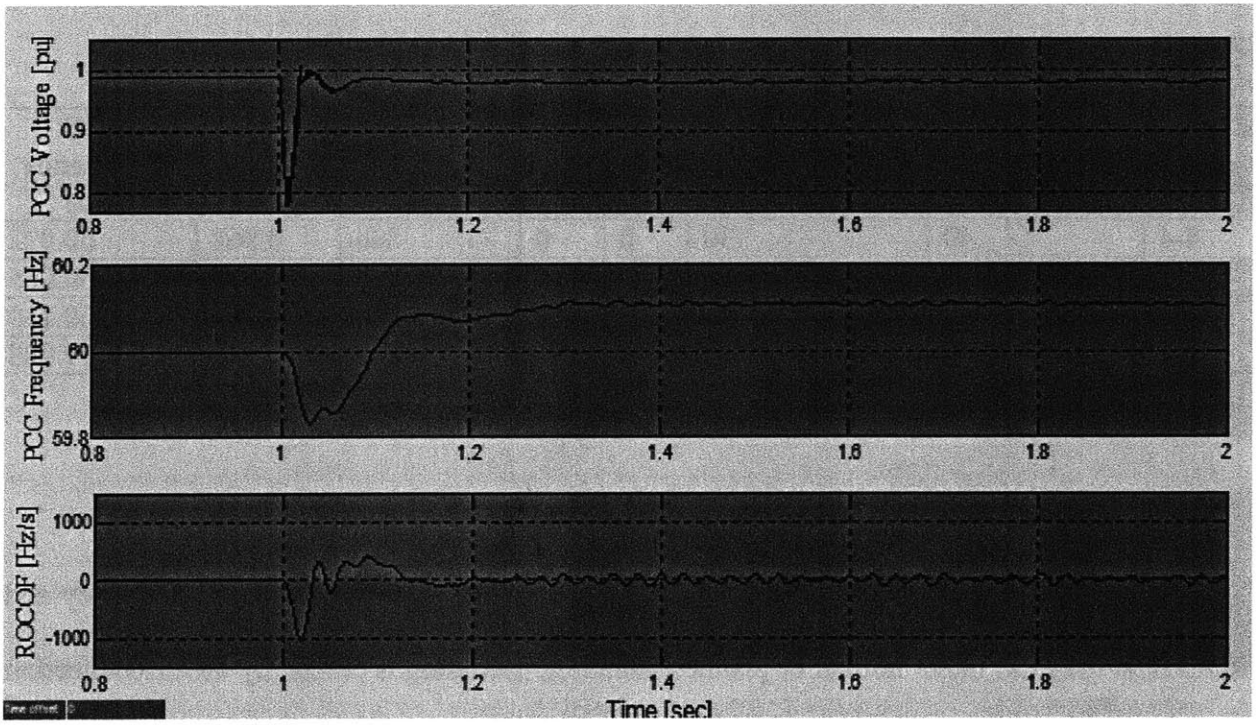

Figure 4-6: Voltage, Frequency and ROCOF subject to 50 kVa Constant Impedance Load

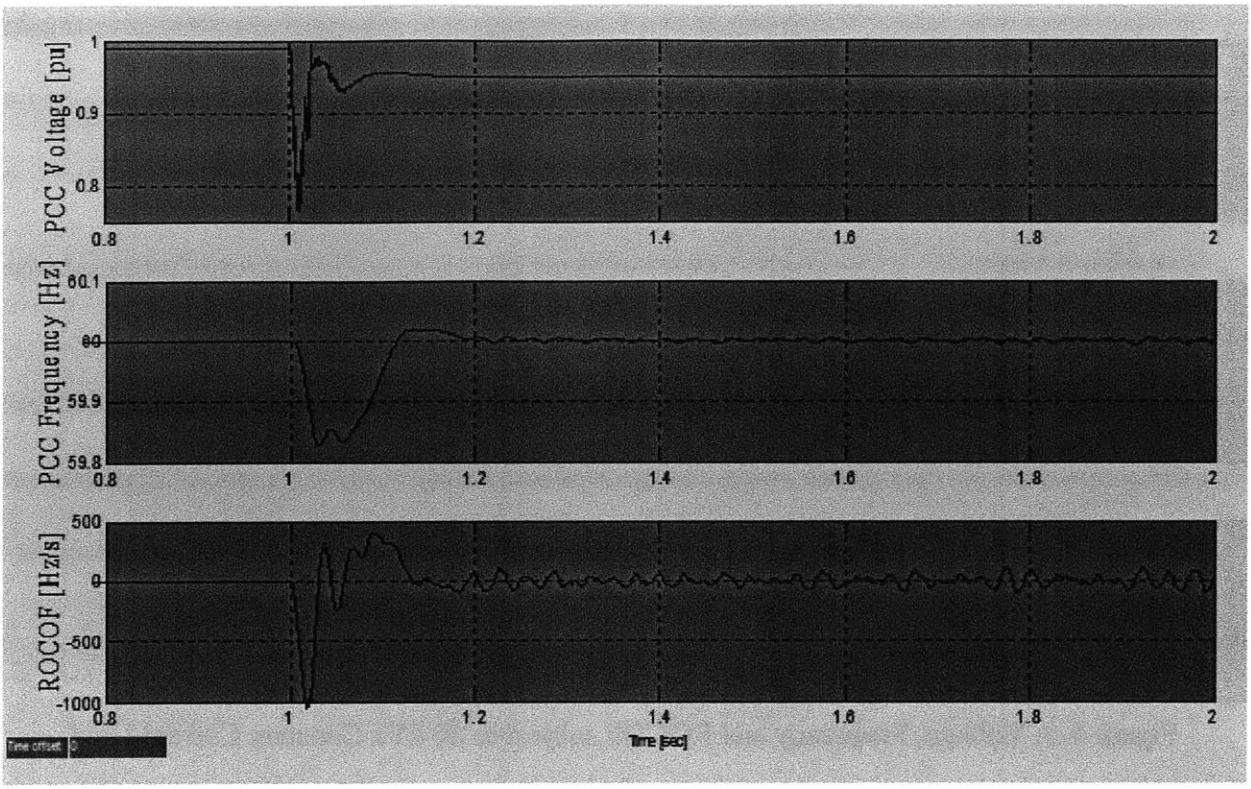

Figure 4-7: Voltage, Frequency and ROCOF subject to Constant Power and IM Loads

Figure No.	Static Loads Total Real Power (kW)	Static Loads Total Reactive Power (kVar)	NP	NQ	IM Loads	PCC Voltage (p.u.)	PCC Frequency (Hz)
4-4	40	30	0	0	No	0.962	60.022
4-5	40	30	1	1	No	0.974	60.065
4-6	40	30	2	2	No	0.981	60.110
4-7	28	21	0	0	Yes	0.946	59.988

Figure 4-8: Planned Islanding Steady-State Values

Figures 4-4 through 4-7 examine the response of the microgrid voltage, frequency and ROCOF at the PCC under normal or planned islanding. Islanding is caused by the disconnection of the grid at time equal to one second.

During planned islanding, the microgrid PCC voltage and frequency deviations depend on the inverter controller settings, the active and reactive power mismatch of the loads, and the characteristics of the loads [16]. For all simulations, the inverter control system was set to deliver maximum real power at the rated line frequency of 60 Hz and to deliver zero reactive power at the rated line voltage magnitude of 1 pu. The active and reactive power mismatch was also held constant for all simulations. The power factor for all microgrid loads was approximately 0.8. The microgrid load characteristics were varied for each plot as follows: figure 4-4 contains only constant power loads connected to the microgrid, figure 4-5 contains only constant current loads, figure 4-6 contains only constant impedance loads and figure 4-7 contains a mixture of constant power loads with IM loads. The microgrid loads in figures 4-4 through 4-6 use the exponential static load models described in section 3.1 and the microgrid loads in figure 4-7 use a combination of the constant power exponential static load model and IM load model described in section 3.2. The total load amount for each case is just under 50kVA. The parameters for the IM loads are given in Appendix B-3.

During the time period before islanding (during grid-connected operation) the microgrid PCC voltage and frequency are controlled by the IEEE-13 voltage and frequency at node 680 for all four simulations cases. The node 680 per unit voltage magnitude is approximately 1and the frequency is at 60 Hz. Therefore, the microgrid inverter operates at unity power factor, supplying 40 kW of real power and approximately zero reactive power. In theory, if the voltage magnitude at node 680 operates at a value lower than 1 pu, the microgrid DG unit must supply reactive power. Conversely, if the voltage magnitude at node 680 is greater than 1 pu, the microgrid DG unit will absorb reactive power.

Once the breaker is opened at time equal to 1 second, the microgrid must supply the 30kVar required by the loads. Therefore, the reactive power requirement of the inverter is essentially a *step* at the time of islanding due to the power mismatch. As discussed before, since the reactive power is linked with the microgrid voltage, we see a PCC voltage transient immediately after grid disconnection. The transient settles to a steady-state equilibrium voltage value after approximately 200 milliseconds. The PCC frequency suffers a transient due to a slight real power decrease during grid disconnection. This real power deviation is quickly restored by the controller and the frequency settles after approximately 200 milliseconds.

The microgrid voltage and frequency values at equilibrium differ slightly with the microgrid loads. Figure 4-8 is a table summarizing the steady-state values of PCC voltage and PCC frequency for each plot after the transient behavior. From figure 4-8 we can see that the voltage magnitude deviations from 1pu increase as the NP and NQ values of the exponential load model decrease. Moreover, the frequency deviations from 60Hz decrease as NP and NQ values of the exponential load model decrease. Therefore, constant power loads will cause greater voltage deviations but lower frequency deviations than constant impedance loads. Nevertheless, during planned islanding the microgrid voltage and frequency remain within acceptable operational limits, even in the presence of IM loads. Due to the robustness of the inverter control system, proper microgrid operation can be achieved under normal islanding conditions.

4.3 Fault Provoked Islanding Simulations

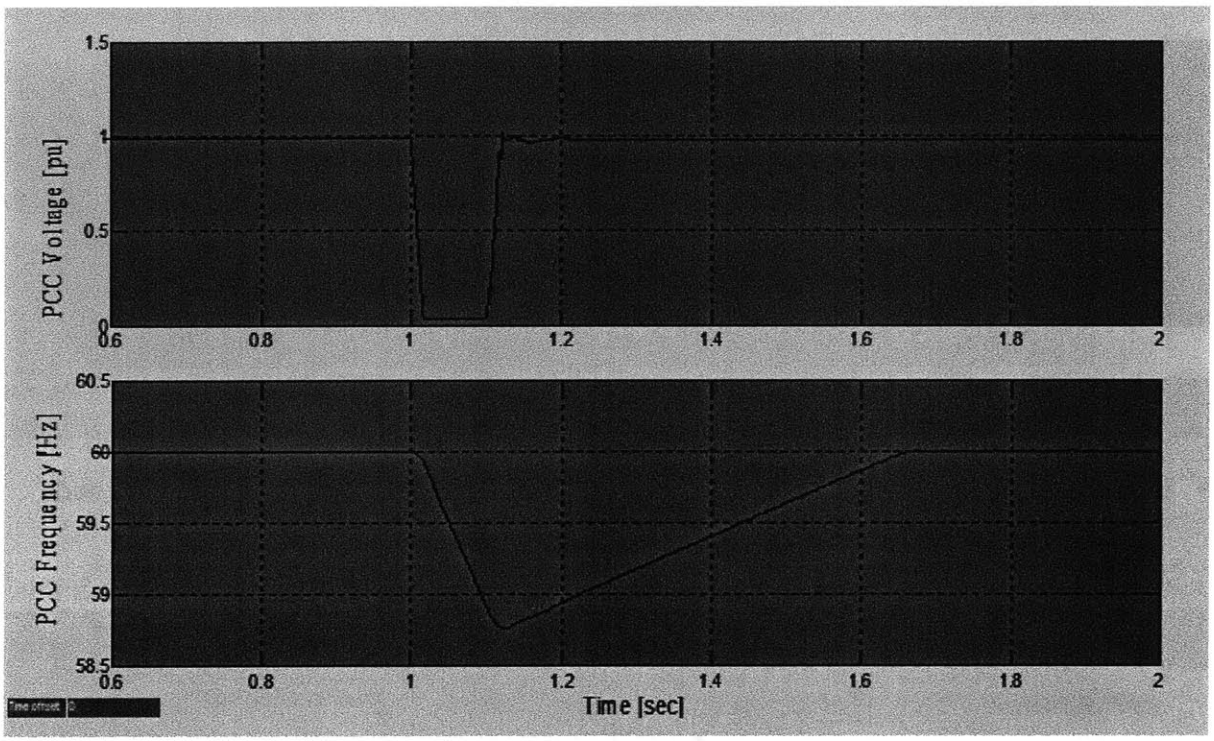

Figure 4-9: Voltage and Frequency subject to Constant Power Loads

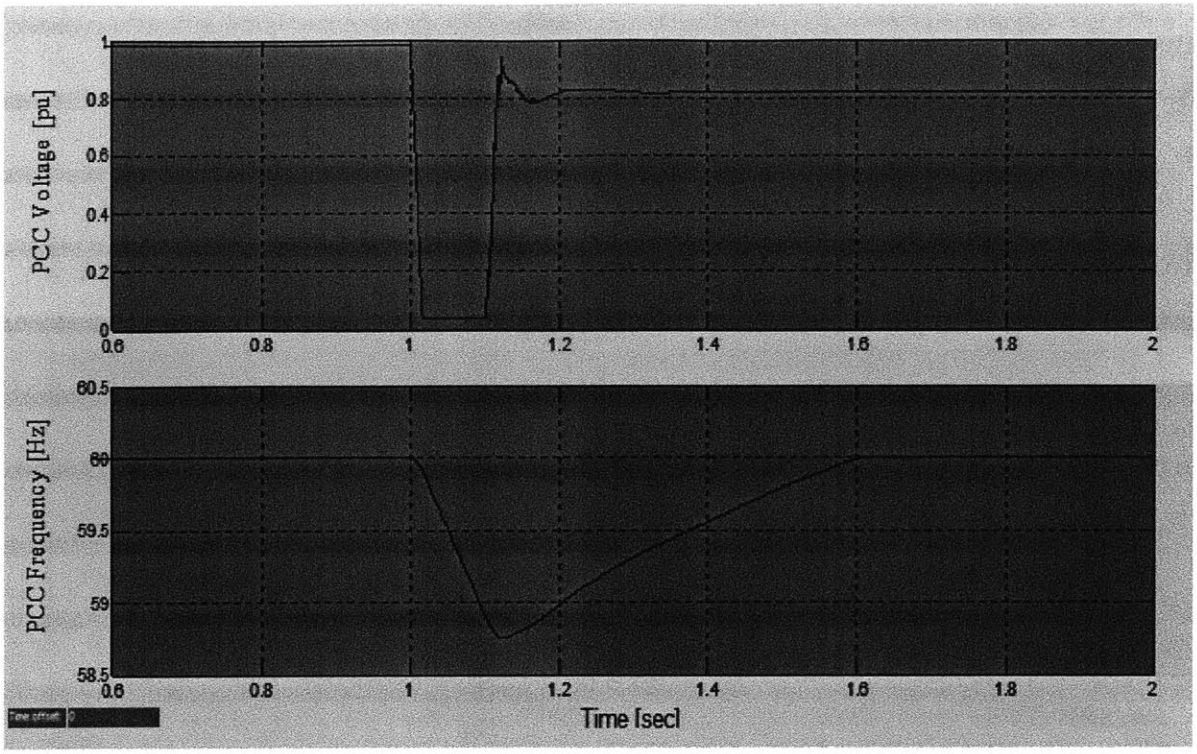

Figure 4-10: Voltage and Frequency subject to 75% Constant Power and 25% IM Loads

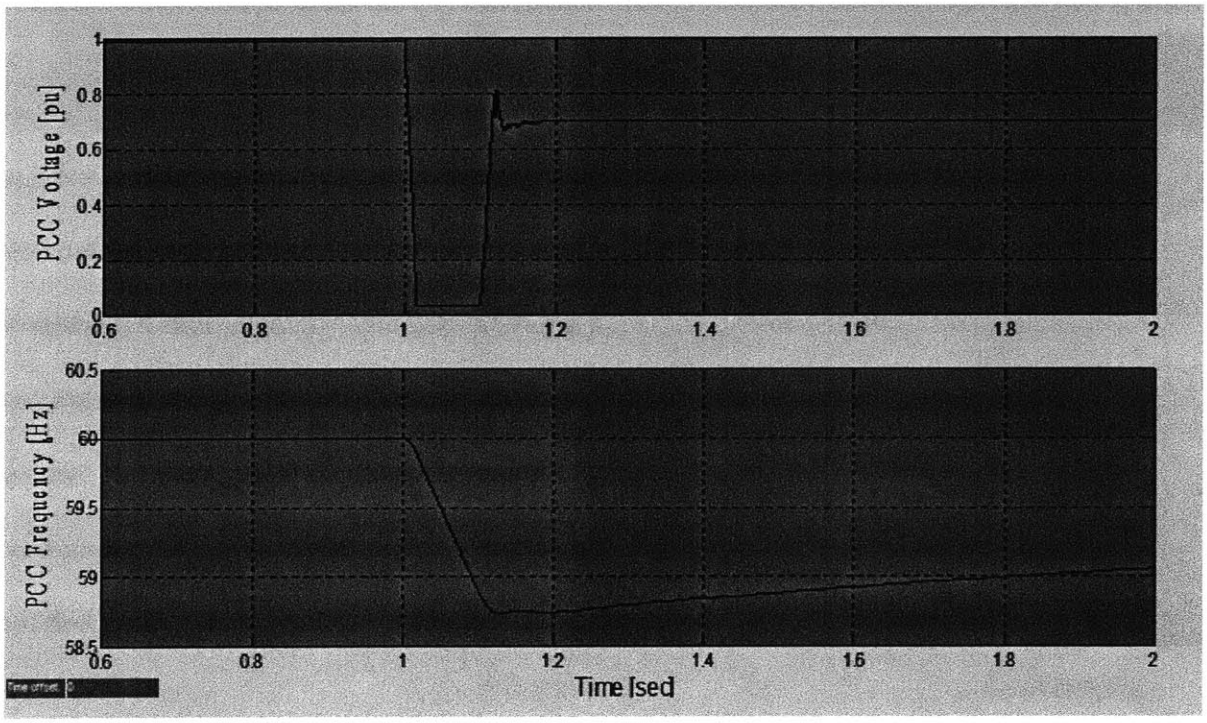

Figure 4-11: Voltage and Frequency subject to 50% Constant Power and 50% IM Loads

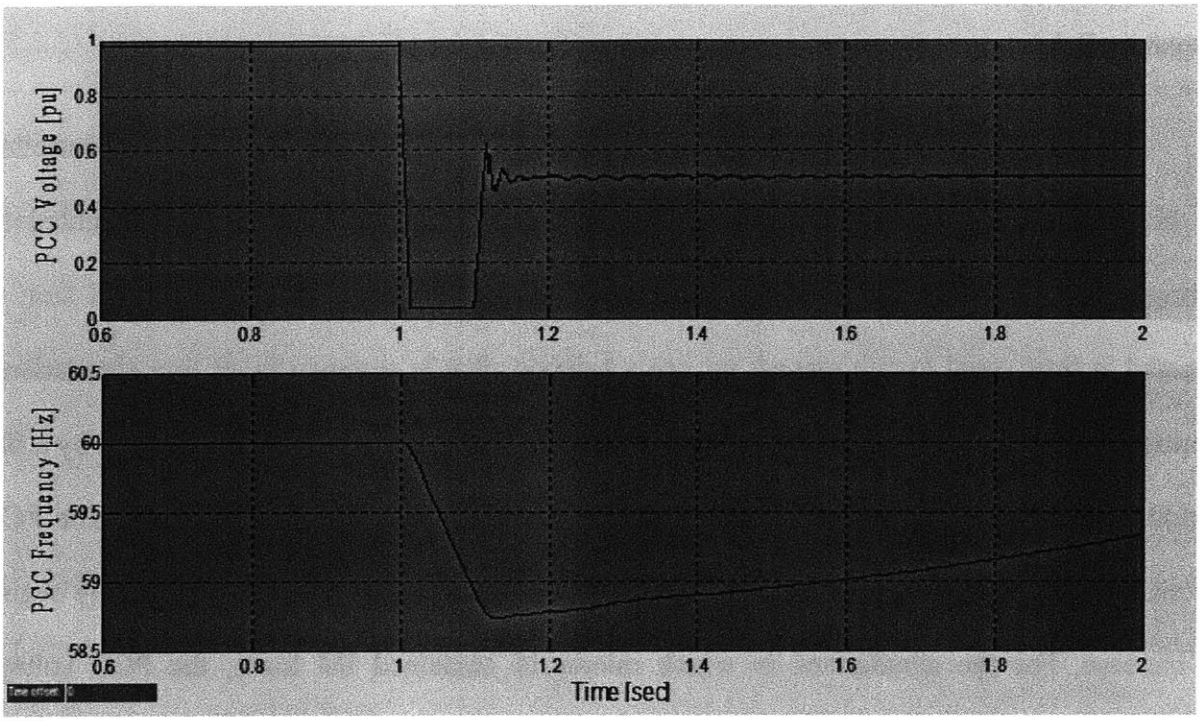

Figure 4-12: Voltage and Frequency subject to 25% Constant Power and 75% IM Loads

Figures 4-9 through 4-12 examine the response of the microgrid voltage and frequency at the PCC under abnormal or unplanned islanding due to a three phase symmetrical ground fault. When islanding occurs the grid is disconnected and the fault is cleared after 0.1 seconds.

As for the planned islanding simulations, the inverter control system was set to deliver maximum real power at the rated line frequency of 60 Hz and to deliver zero reactive power at the rated line voltage magnitude of 1 pu. The microgrid load composition is varied for each plot as follows: figure 4-9 contains only constant power loads, figure 4-10 contains 75% constant power loads and 25% IM loads, figure 4-11 contains 50% constant power loads and 50% IM loads and figure 4-12 contains 25% constant power loads and 75% IM loads. The total load

amount for each case is just under 50kVa. The parameters for the IM loads are given in Appendix B-3.

During grid-connected operation the microgrid PCC voltage and frequency are controlled by the voltage and frequency at node 680. This operation is similar to the previous simulations during which the microgrid inverter operated at unity power factor. Once the ground fault is initiated at time equal to one second, we see a behavior that is common in all four simulations. During the fault the PCC voltage magnitude exhibits a sharp decrease. This is followed by a flat period, a sharp increase once the fault is cleared and then the value finally settles. The PCC frequency exhibits a gradual decrease during the fault. Once the fault is cleared it slowly begins to increase. For the simulations in which microgrid contained IM loads, the PCC voltage magnitude did not recover to pre-fault conditions and the PCC frequency either took longer to recover or never recovered to pre-fault conditions at all. Whereas the simulation that contained only static loads was able to recover its pre-fault PCC voltage and frequency values.

When the balanced ground fault occurs, the voltage at each phase of the line begins to sag. If the IM loads are present, this voltage sag will cause electrical and mechanical transients in the IM. Since the time electrical time constant of the IM is much smaller than the mechanical time constant, the electrical torque in the machine is reduced while the mechanical torque remains relatively the same. The electrical torque is reduced by the square of the voltage sag magnitude root mean square value. Energy is dissipated through the internal rotor circuitry, such as the magnetizing inductance and through the faulted path. As the electrical torque is reduced, the motor speed is reduced from the nominal speed as shown in figure 4-13, 4-14, and 4-15. This increases the slip of the machine and the reactive power demand is greatly increased. The longer the fault duration, the more the IM speed will decrease and the more reactive power it will draw.

Moreover, the more the speed is decreased, the lower the maximum torque the IM can produce. If the mechanical torque imposed on the IM is higher than the maximum torque it can produce at the new operating point, IM stalling is expected to occur.

In general, microgrid voltage and frequency recovery to pre-fault conditions is highly sensitive to the duration of the fault, which is why the IEEE St. 1547 requires fast fault detection and grid disconnection. Once the grid is disconnected and the fault is cleared the voltage begins to recover. In figure 4-9, the simulation with only static loads connected to the microgrid, we clearly see a successful recovery of PCC voltage and frequency to pre-fault conditions. However, the case when IM loads are present is different. After fault clearance, current IM speed remains lower than its nominal speed value and therefore begins to reaccelerate. The reacceleration process leads to large currents being drawn to build up flux in the IM and reach nominal speed. Figure 4-15 shows an IM load that recovers its nominal speed successfully and figure 4-14 shows an IM load that cannot recover its nominal speed after fault clearance. Clearly, the PCC voltage is affected by this reacceleration process. This can be seen in the fact that figures 4-10 through 4-12 do not recover pre-fault conditions. Furthermore, the reacceleration time increases with the time duration of the fault as the IM slip increases and the IM loads cannot recover to their nominal operating point. In all the cases simulated in which the microgrid contained IM loads, the reacceleration time became very long and post-fault PCC voltage restoration to pre-fault values was not possible. Lastly, figures 4-10 through 4-12 show that the recovery of microgrid voltage is also dependent on the percentage of IM loads connected to the microgrid in comparison to the total load. The larger the percentage of IM loads connected to the microgrid, the lower the post-fault voltage value will be. The microgrid frequency also takes longer to stabilize and like the voltage, does not recover its pre-fault values as the presence of IM loads

connected to the microgrid becomes significant. Note that in the absence of IM loads connected to the microgrid (figure 4-9), the control system is able to recover the voltage and frequency to pre-fault levels.

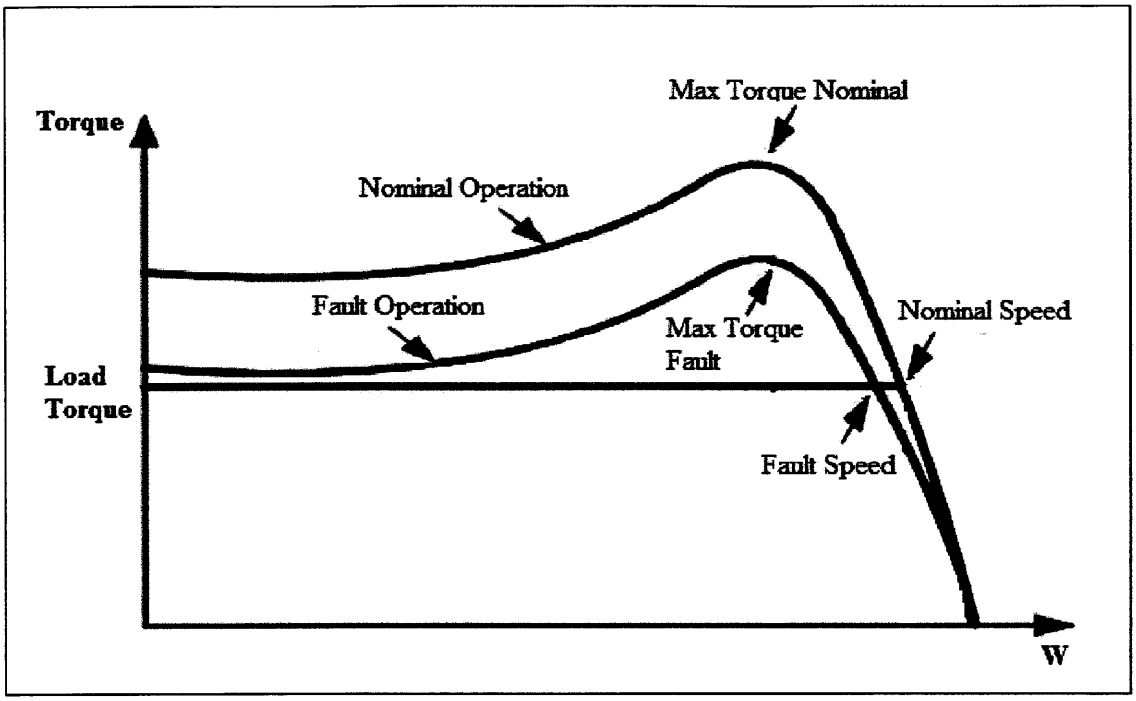

Figure 4-13: IM Torque Speed Curve Showing Nominal and Fault Operation

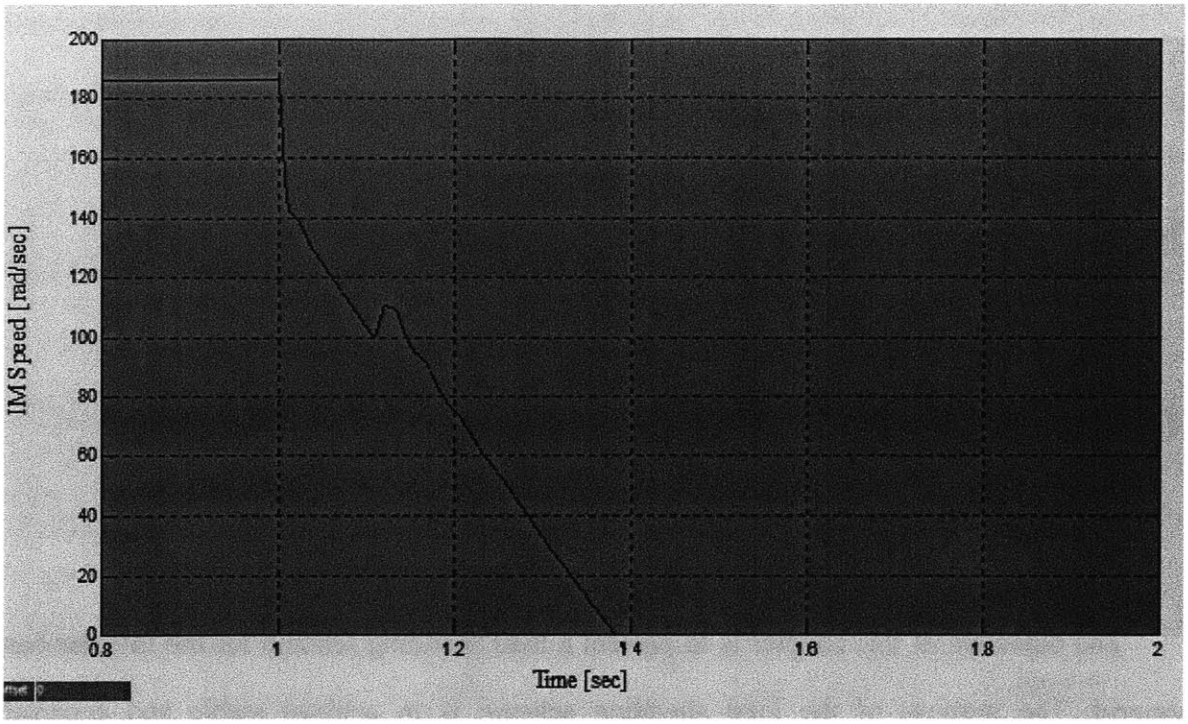

Figure 4-14: IM Speed Showing Speed Decline after Fault Clearance

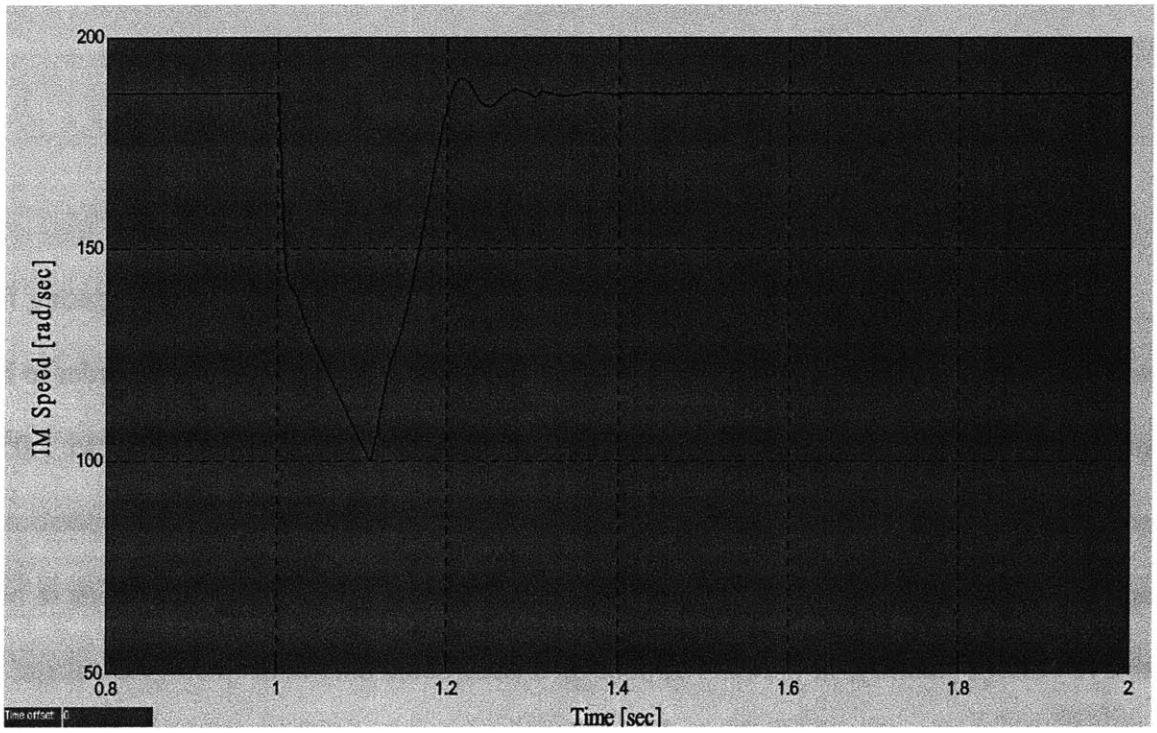

Figure 4-15: Typical IM Speed Showing Recovery after Fault Clearance

Chapter 5

Load Shedding Scheme

The objective of this chapter is to present a load shedding scheme for the inverter-based microgrid. The purpose of the load shedding scheme is to achieve stable and acceptable microgrid voltage and frequency values after fault provoked islanding occurs and in the presence of induction motor loads.

5.1 Load Shedding Basics

Since the presence of IM loads greatly degrades post fault microgrid voltage during fault provoked islanding, an under-voltage load shedding scheme can be implemented in order to help achieve stable and acceptable values, which are generally in the range of .95pu to 1.05pu. Appropriate post fault microgrid voltage and frequency is vital to achieve proper operation of voltage and frequency sensitive loads. Even though it is undesirable to disconnect loads in order to achieve voltage stability, in the case of poor or unacceptable post fault microgrid voltage and frequency, sensitive loads can suffer damage or stop working wholly when not disconnected.

This is one argument for the use of load shedding to improve post fault stability. Another argument for load shedding is that it is relatively low cost to implement.

The objectives of the load shedding scheme are to shed the minimum amount of load possible, by avoiding unnecessary load shedding actions, but still achieve the desired microgrid voltage.

5.2 Microgrid Load Shedding

The strategy for this load shedding scheme will be to shed load at a specific point during the reacceleration period. From figure 4-14, which depicts the case in which IM fault speed does not recover to nominal speed, we can see that there is a slight increase in the speed after the fault is cleared before it drops to low values and becomes unstable. The time at which this local speed peak occurs would be an appropriate initial load shedding point. Clearly, if at this point in the IM reacceleration period the speed successfully increases from the fault speed back to nominal speed, we do not have to load shed as acceptable post-fault value will be achieved.

This point of interest corresponds to the post-fault value of the PCC voltage magnitude plot right after the increase in voltage due to the fault clearance. Using as a reference the value to which the PCC voltage magnitude settles after the fault clearance, the amount of load to be shed can be determined. Obviously, if the PCC voltage magnitude is within acceptable limits after the fault, no load would be shed. The PCC voltage magnitude will also be a measure of the percentage of IM loads connected to the microgrid with respect to the total loads. As discussed in

chapter 4, the larger the presence of IM loads, the lower the post-fault PCC voltage magnitude value will be.

Since the proposed load shedding scheme will depend on the percentage of IM loads connected to the microgrid, the scheme will have two load shedding strategies. The first strategy will apply to post fault microgrid voltage values greater than 0.6 pu and the second strategy will apply to post fault microgrid voltage values at 0.6 pu or lower.

For the first case, if the percentage of IM loads connected to the microgrid total 50 percent or less of the total load, the post fault microgrid voltage will likely be no lower than 0.6 pu. Therefore, an amount totaling 5 percent of the total load shall be shed in IM load with a delay time of 400 milliseconds until an acceptable voltage level is reached. If the percentage of IM loads connected to the microgrid is greater than 50 percent of the total load, the post fault voltage will likely be lower than 0.6. For this second case, an amount totaling 10 percent of the total load shall be shed in IM load with a delay time of 400 milliseconds until a voltage level of 0.6 pu is reached. Once this level is reached, the strategy used for the first case is adopted and 5 percent of the total load shall be shed in IM load with a delay time of 400 milliseconds until an acceptable voltage level is reached.

Figure 5-1 summarizes the load shedding scheme and figure 5-2 and 5-3 show a simulation for each load shedding case.

	Case 1	Case 2*
Post Fault Voltage [pu]	Greater than 0.6	Less than or equal to 0.6
IM Load Shed	5% of total load	10% of total load
Delay Time	400 msec	400 msec

Figure 5-1: Load Shedding Scheme

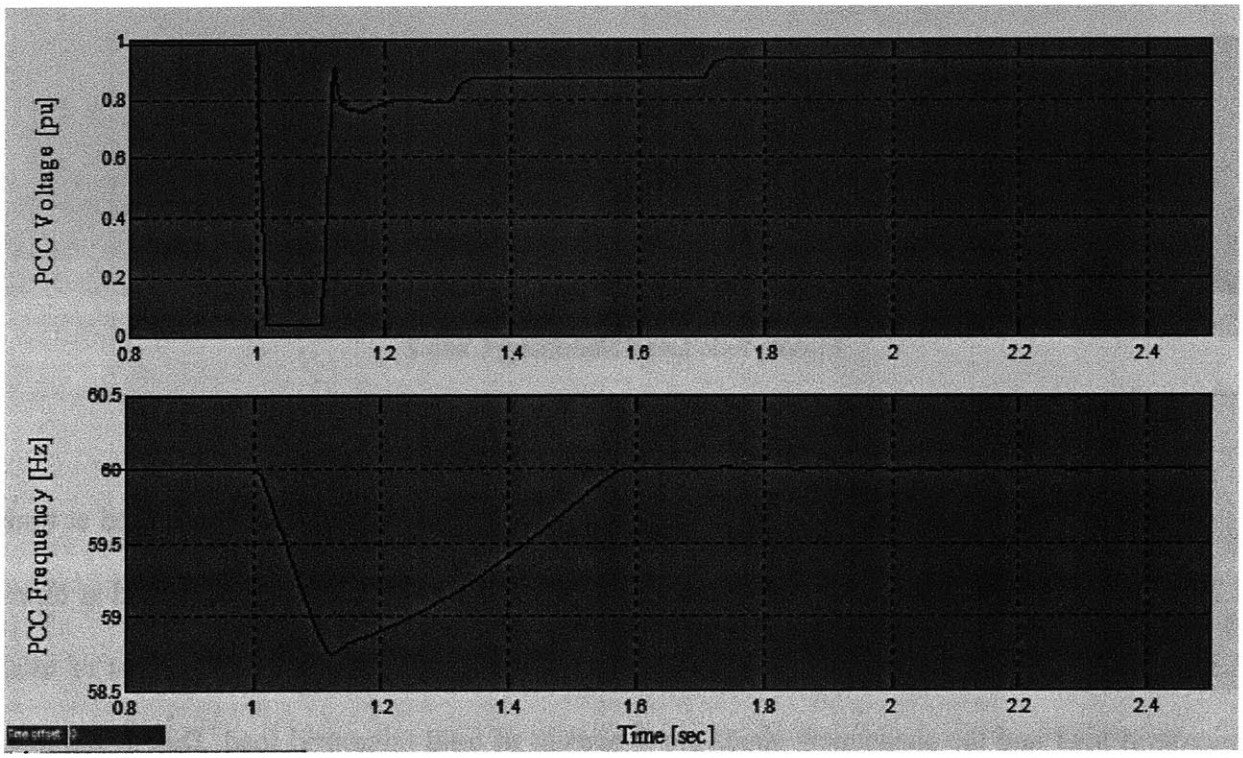

Figure 5-2: Load Shedding Case 1

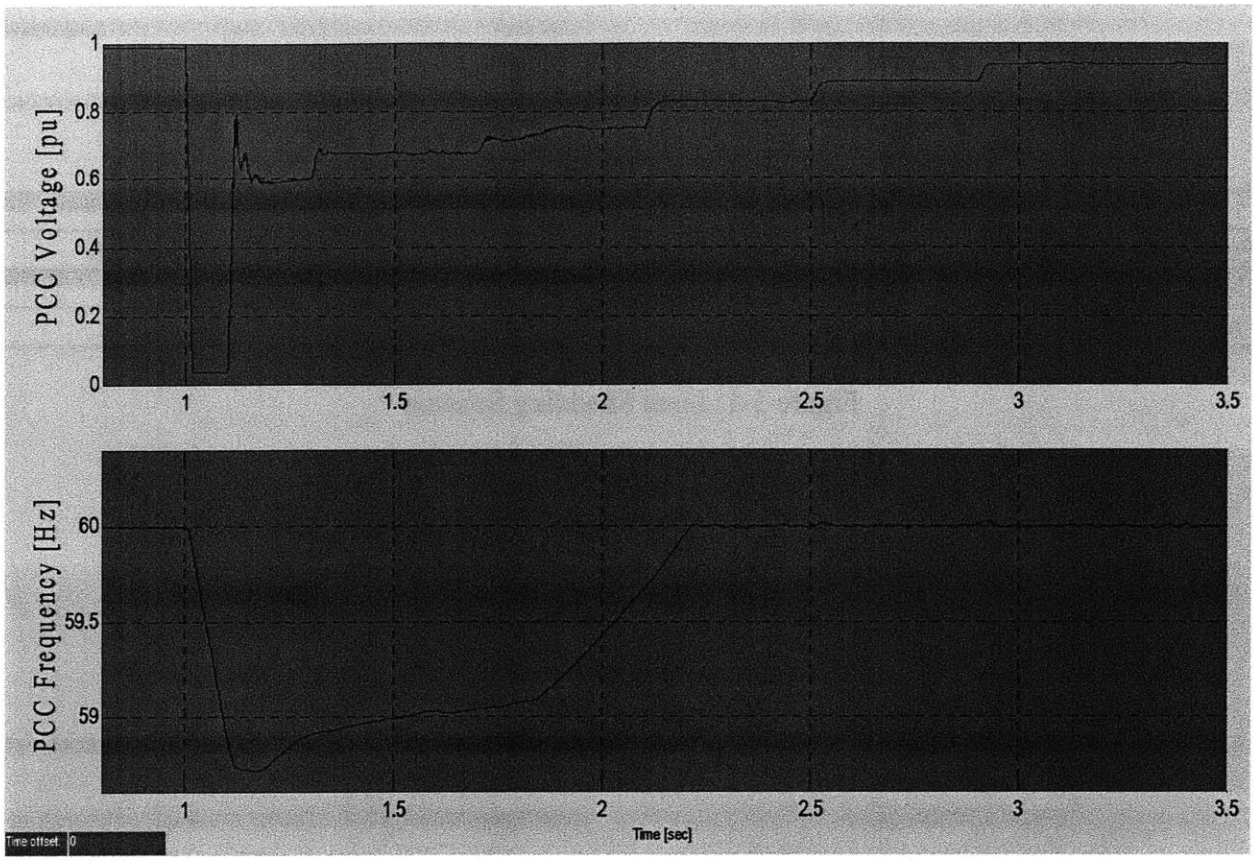

Figure 5-3: Load Shedding Case 2

Figure 5-2 shows that IM loads totaling 5 percent of full microgrid load are shed at time 1.3 seconds and then again at time 1.7 seconds. Figure 5-3 shows IM loads being shed at times 1.3, 1.7, 2.1, 2.5 and 2.9 seconds. The first IM load shed at 1.3 seconds is 10 percent of total microgrid load and the subsequent sheds are 5 percent of total microgrid load. Due to the load shedding actions the post-fault microgrid voltage and frequency are improved.

Chapter 6

Conclusion

6.1 Summary

A load shedding scheme was developed in order to improve the PCC voltage and frequency of an inverter-based microgrid after symmetrical three-phase ground faults. The load shedding scheme was developed using the *SimPowerSystems* simulation environment of *MatLab Simulink*. In chapter 2, the IEEE-13 bus distribution feeder was modeled to behave as a sample grid. The microgrid was connected to node 680, where various normal and fault provoked islanding conditions were generated. Models for a variety of static loads and induction motor loads for the microgrid were developed in chapter 3. The beginning of chapter 4 presents the microgrid model, including the control system and filters. The rest of the chapter is dedicated to normal and fault provoked islanding conditions simulations. In chapter 5, the load shedding scheme is presented.

Based on simulation results, it is evident that there are large differences in the transient behavior of normal and fault provoked islanding. Under fault provoked islanding, post-fault

microgrid voltage and frequency recovery to pre-fault conditions is highly sensitive to the duration of the fault and the presence of IM loads. As the percentage of IM loads to total microgrid loads is increased, the post-fault microgrid voltage has a lower recovery. Load shedding was used post fault to aid in microgrid voltage and frequency recovery to acceptable operational limits.

Appendix A

IEEE-13 Distribution Test Feeder
(http://ewh.ieee.org/soc/pes/dsacom/testfeeders/index.html)

A-1: Transmission Line Configuration Data

Overhead Line Configuration Data:

Config.	Phasing	Phase	Neutral	Spacing
		ACSR	ACSR	ID
601	B A C N	556,500 26/7	4/0 6/1	500
602	C A B N	4/0 6/1	4/0 6/1	500
603	C B N	1/0	1/0	505
604	A C N	1/0	1/0	505
605	C N	1/0	1/0	510

Underground Line Configuration Data:

Config.	Phasing	Cable	Neutral	Space ID
606	A B C N	250,000 AA, CN	None	515
607	A N	1/0 AA, TS	1/0 Cu	520

Line Segment Data:

Node A	Node B	Length(ft.)	Config.
632	645	500	603
632	633	500	602
633	634	0	XFM-1
645	646	300	603
650	632	2000	601
684	652	800	607
632	671	2000	601
671	684	300	604
671	680	1000	601
671	692	0	Switch
684	611	300	605
692	675	500	606

Line Impedance:

Configuration 601:

```
            Z (R +jX) in ohms per mile
 0.3465   1.0179    0.1560   0.5017    0.1580   0.4236
                    0.3375   1.0478    0.1535   0.3849
                                       0.3414   1.0348
           B in micro Siemens per mile
             6.2998    -1.9958    -1.2595
                        5.9597    -0.7417
                                   5.6386
```

Configuration 602:

```
            Z (R +jX) in ohms per mile
0.7526   1.1814    0.1580   0.4236    0.1560   0.5017
                    0.7475   1.1983    0.1535   0.3849
                                       0.7436   1.2112
           B in micro Siemens per mile
             5.6990    -1.0817    -1.6905
                        5.1795    -0.6588
                                   5.4246
```

Configuration 603:

```
          Z (R +jX) in ohms per mile
 0.0000  0.0000   0.0000  0.0000   0.0000  0.0000
                  1.3294  1.3471   0.2066  0.4591
                                   1.3238  1.3569
         B in micro Siemens per mile
           0.0000    0.0000    0.0000
                     4.7097   -0.8999
                               4.6658
```

Configuration 604:

```
          Z (R +jX) in ohms per mile
 1.3238  1.3569   0.0000  0.0000   0.2066  0.4591
                  0.0000  0.0000   0.0000  0.0000
                                   1.3294  1.3471
         B in micro Siemens per mile
           4.6658    0.0000   -0.8999
                     0.0000    0.0000
                               4.7097
```

Configuration 605:

```
          Z (R +jX) in ohms per mile
 0.0000  0.0000   0.0000  0.0000   0.0000  0.0000
                  0.0000  0.0000   0.0000  0.0000
                                   1.3292  1.3475
         B in micro Siemens per mile
           0.0000    0.0000    0.0000
                     0.0000    0.0000
                               4.5193
```

Configuration 606:

```
          Z (R +jX) in ohms per mile
0.7982  0.4463   0.3192  0.0328   0.2849 -0.0143
                 0.7891  0.4041   0.3192  0.0328
                                  0.7982  0.4463
         B in micro Siemens per mile
          96.8897    0.0000    0.0000
                    96.8897    0.0000
                              96.8897
```

Configuration 607:

```
          Z (R +jX) in ohms per mile
 1.3425  0.5124   0.0000  0.0000   0.0000  0.0000
                  0.0000  0.0000   0.0000  0.0000
                                   0.0000  0.0000
         B in micro Siemens per mile
          88.9912    0.0000    0.0000
                     0.0000    0.0000
                               0.0000
```

A-2: Transformer Data

Transformer Data:

	kVA	kV-high	kV-low	R - %	X - %
Substation:	5,000	115 - D	4.16 Gr. Y	1	8
XFM -1	500	4.16 – Gr.W	0.48 – Gr.W	1.1	2

Regulator Data:

Regulator ID:	1		
Line Segment:	650 - 632		
Location:	50		
Phases:	A - B -C		
Connection:	3-Ph,LG		
Monitoring Phase:	A-B-C		
Bandwidth:	2.0 volts		
PT Ratio:	20		
Primary CT Rating:	700		
Compensator Settings:	Ph-A	Ph-B	Ph-C
R - Setting:	3	3	3
X - Setting:	9	9	9
Volltage Level:	122	122	122

A-3: Shunt Capacitor Data

Node	Ph-A	Ph-B	Ph-C
	kVAr	kVAr	kVAr
675	200	200	200
611			100
Total	200	200	300

A-4: Loads

Spot Load Data:

Node	Load	Ph-1	Ph-1	Ph-2	Ph-2	Ph-3	Ph-3
	Model	kW	kVAr	kW	kVAr	kW	kVAr
634	Y-PQ	160	110	120	90	120	90
645	Y-PQ	0	0	170	125	0	0
646	D-Z	0	0	230	132	0	0
652	Y-Z	128	86	0	0	0	0
671	D-PQ	385	220	385	220	385	220
675	Y-PQ	485	190	68	60	290	212
692	D-I	0	0	0	0	170	151
611	Y-I	0	0	0	0	170	80
	TOTAL	1158	606	973	627	1135	753

Distributed Load Data:

Node A	Node B	Load	Ph-1	Ph-1	Ph-2	Ph-2	Ph-3	Ph-3
		Model	kW	kVAr	kW	kVAr	kW	kVAr
632	671	Y-PQ	17	10	66	38	117	68

A-5: Voltage Profile

--- **V O L T A G E P R O F I L E** ---- DATE: 6-24-2004 AT 15:33:12 HOURS ----
SUBSTATION: IEEE 13; FEEDER: IEEE 13

NODE	MAG	ANGLE	MAG	ANGLE	MAG	ANGLE	mi.to SR
	A-N		B-N		C-N		
650	1.0000 at	.00	1.0000 at	-120.00	1.0000 at	120.00	.000
RG60	1.0625 at	.00	1.0500 at	-120.00	1.0687 at	120.00	.000
632	1.0210 at	-2.49	1.0420 at	-121.72	1.0174 at	117.83	.379
633	1.0180 at	-2.56	1.0401 at	-121.77	1.0148 at	117.82	.474
XFXFM1	.9941 at	-3.23	1.0218 at	-122.22	.9960 at	117.35	.474
634	.9940 at	-3.23	1.0218 at	-122.22	.9960 at	117.34	.474
645			1.0329 at	-121.90	1.0155 at	117.86	.474
646			1.0311 at	-121.98	1.0134 at	117.90	.530
671	.9900 at	-5.30	1.0529 at	-122.34	.9778 at	116.02	.758
680	.9900 at	-5.30	1.0529 at	-122.34	.9778 at	116.02	.947
684	.9881 at	-5.32			.9758 at	115.92	.815
611					.9738 at	115.78	.871
652	.9825 at	-5.25					.966
692	.9900 at	-5.31	1.0529 at	-122.34	.9777 at	116.02	.852
675	.9835 at	-5.56	1.0553 at	-122.52	.9758 at	116.03	.947

p 1

---------- **VOLTAGE REGULATOR DATA** ---- DATE: 6-24-2004 AT 15:33:16 HOURS --
SUBSTATION: IEEE 13; FEEDER: IEEE 13

[NODE]	[VREG]	[SEG]	[NODE]	MODEL	OPT	BNDW
650	RG60	632	632	Phase A & B & C, Wye	RX	2.00

PHASE	LDCTR	VOLT HOLD	R-VOLT	X-VOLT	PT RATIO	CT RATE	TAP
1		122.000	3.000	9.000	20.00	700.00	10
2		122.000	3.000	9.000	20.00	700.00	8
3		122.000	3.000	9.000	20.00	700.00	11

Appendix B

B-1: P_{DG} and Q_{DG} Calculation

The three-phase voltages and currents at the output of the inverter can be measured and related to P_{DG} and Q_{DG} as follows:

$$P_{DG} = V_{Ia} I_{Ia} + V_{Ib} I_{Ib} + V_{Ic} I_{Ic} \quad \text{(B.1)}$$

$$Q_{DG} = \frac{V_{Iab} I_{Ic} + V_{Ibc} I_{Ia} + V_{Ica} I_{Ib}}{\sqrt{3}} \quad \text{(B.2)}$$

Applying Park's Transform to equations B.1 and B.2 we obtain a relation for P_{DG} and Q_{DG} in a rotating coordinate system.

$$P_{DG} = 1.5(V_{Id} I_{Id} + V_{Iq} I_{Iq}) \quad \text{(B.3)}$$

$$Q_{DG} = 1.5(V_{Iq} I_{Id} - V_{Id} I_{Iq}) \quad \text{(B.4)}$$

B-2: PI Controller Parameters

PI_1
K_p : 0.05
K_I : 2

PI_2
K_p : 0.01
K_I : 3

PI_3
K_p : 0.05
K_I : 2

PI_4
K_p : 0.01
K_I : 3

B-3: Induction Motor Parameters

IM #1
Nominal Power: 5HP
Voltage (line-line): 460 Vrms
Frequency: 60 Hz
Stator Resistance: 1.115 Ohm
Stator Inductance: 5.974 mH
Rotor Resistance: 1.083 Ohm
Rotor Inductance: 5.974 mH
Mutual Inductance: 0.2037 H
Inertia: 0.02 $kg \cdot m^2$
Friction Factor: 0.005752 $N \cdot m \cdot s$
Pole Pairs: 2
Mechanical Torque: 15 $N \cdot m$ (constant)

IM #2
Nominal Power: 10HP
Voltage (line-line): 460 Vrms
Frequency: 60 Hz
Stator Resistance: 0.6837 Ohm
Stator Inductance: 4.152 mH
Rotor Resistance: 0.451 Ohm
Rotor Inductance: 4.152 mH
Mutual Inductance: 0.1486 H
Inertia: 0.05 $kg \cdot m^2$
Friction Factor: 0.008141 $N \cdot m \cdot s$
Pole Pairs: 2
Mechanical Torque: 30 $N \cdot m$ (constant)

Bibliography

[1] R. Lassetter, A. Akhil, C. Marnay, et al, "The CERTS MicroGrid Concept", White paper on Integration of Distributed Energy Resources, CERTS, April 2002.

[2] IEEE Std. 929-2000, " IEEE recommended practice for Utility Interface of Photovoltaic (PV) Systems", April 2000.

[3] UL 1741, Static inverter and charge controllers for use in photovoltaic systems, Underwriters Laboratories Inc., Northbrook, IL.

[4] IEEE Standard For interconnecting distributed Resources With Electric Power Systems, IEEE Std. 1547TM, Jul. 21,2003

[5] P. Mahat, Z. Chen, and B. Bak-Jensen, "Review of islanding detection methods for distributed generation," *in Proc. 3rd International Conference on Electric Utility Deregulation and Restructuring and Power Technologies*, pp. 2743 – 2748, 6-9 April 2008.

[6] M. C. Chandorkar, D. M. Divan, and R. Adapa, "Control of parallel connected inverters In standalone AC supply systems," *IEEE Trans. Ind. Appl.*, vol. 29, no. 1, pp. 136–143, Jan.–Feb. 1993.

[7] J. A. P. Lopes, C. L. Moreira, and A. G. Madureira, "Defining control strategies for microgrids islanded operation," *IEEE Trans. Power Syst.*, vol. 21, no. 2, pp. 916–924, May 2006.

[8] B. Delfino, S. Massucco, A. Morini, P. Scalera, F. Silvestro, "Implementation and Comparison of Different Under Frequency Load-Shedding Schemes", IEEE Summer Meeting 2001, Vancouver (Canada), 15-19 July 2001

[9] P.M. Anderson, M. Mirheydar, "An adaptive method for setting under frequency load shedding relays", IEEE Transactions on Power Systems, VOL.7, NO.2, May 1992, pp.647-655

[10] W. H. Kersting, "Radial distribution test feeders," in *Proc. Power Engineering Society Winter Meeting*, Columbus, OH, 2001.

[11] Mathworks, *Simulink–Dynamic System Simulation for Matlab*, Natick, MA:

The Mathworks Inc, November 2000.

[12] Hydro-Québec, TransÉnergie Technologies, *SimPowerSystems for Use with Simulink,* Natick, MA: The Mathworks Inc, February 2003.

[13] E. Vaahedi, H.M. Zein El-Din, W.W. Price, "Dynamic Load Modeling in Large Scale Stability Studies," IEEE Trans. PWRS-3, pp. 1039-45, 1988

[14] IEEE Task Force on Load Representation for Dynamic Performance, 'Load representation for dynamic performance analysis'. IEEE Transactions on Power Systems, Vol.8, No.2, pp. 472-482, May 1993.

[15] Krause, P.C., O. Wasynczuk, and S.D. Sudhoff, *Analysis of Electric Machinery*, IEEE Press, 2002.

[16] H.H. Zeineldin, J.L. Kirtley, Jr., "Micro-grid operation of inverter based distributed generation with voltage and frequency dependent loads", Power & Energy Society General Meeting, pp. 1-6, 26-30 July 2009.

[17] J.V. Milanovic, M.T. Aung, S.C. Vegunta, The Influence of Induction Motors on Voltage Sag Propagation, *IEEE Transactions on PD*, Vol.23, No.2, April 2008, pp. 1063 – 1071.